**CLICdp-Note-2015-002**
**22 January 2015**

# Mechanical integration studies for the CLIC vertex and inner tracking detectors

M.A. Villarejo Bermudez*, F. Duarte Ramos†, H. Gerwig†

* *IFIC Valencia, Spain,* † *CERN, Switzerland*

## Abstract

Since the publication of the CLIC Conceptual Design Report, work has proceeded in order to establish a preliminary mechanical design for the innermost CLIC detector region. This note proposes a design for the main Carbon-Fibre Reinforced Polymer (CFRP) structural elements of the inner detectors, for the beam pipe and their supports. It also describes an assembly sequence for the integration of the sensors and the mechanical components. Mechanical simulations of different structural elements and a material budget estimation are appended. Details of a proposed cabling layout for all the subdetectors are included.

# 1 Introduction

This technical note describes the support structures and the assembly sequence proposed for the innermost detectors (vertex detector and inner tracking layers) of a Compact Linear Collider (CLIC) experiment, studied here for the example of the CLIC_ILD detector concept [1]. The proposed design is compatible with the routing of services and the proposed air cooling strategy [2]. The mechanical components introduced in this note are also compatible with the sensor positions used in the physics simulations. While most of the sensor layout is taken from the Conceptual Design Report (CDR), the more recent "petal" layout is used for the vertex endcap disks. The design tries to minimise the static deformations due to the own weight of the different components and dynamic deformations due to the vibrations produced by air cooling. Another important goal of the proposed design is to ensure a low material budget, i.e. to minimise the effect of the mechanical components on the physics performance.

In section 2 an overview of the proposed layout with its main mechanical support structures is given. An overview of the sub-detectors in the inner region, showing their geometry and position, is presented in section 2.1. Section 2.2 details all the composite mechanical structures that support the sensors. Section 2.3 focuses on the beam pipe design and its integration. The description of the assembly sequence is given in section 3. Conclusions are given in section 4, with a summary of the main issues and questions to be addressed in future work.

Numerical simulations for several of the Carbon-Fibre Reinforced Polymer (CFRP) structures have been performed, and the results are shown in Appendix A. A preliminary static and a buckling study of the beam pipe has been performed in order to validate the design (Appendix B). Appendix C gives details of a proposed cabling layout for all the subdetectors, compatible with the assembly scheme and optimised in terms of material budget. In Appendix D, the material budget of the innermost region is calculated and compared to the one used in the physics simulation presented in the CDR. Appendix E provides a list of acronyms used throughout this note.

# 2 Components

In this section, the layout and design of the CLIC_ILD innermost region and its support structures is presented. First, the CDR layout for the vertex and inner tracker sensors is summarized, and the main mechanical structures needed to support the sensors are described. Naming conventions as used throughout this document are introduced. In the second subsection, each of the CFRP support structures is described in detail. The conceptual design of the beam pipe and related shielding is presented in the third subsection.

## 2.1 Inner region detector layout

The layout used in the physics simulations of the CLIC_ILD innermost region consists of a pixel vertex detector and an inner silicon tracker [3]. The vertex detector is composed of three nearly cylindrical concentric layers of double-sided staves (VXBD) and three double-sided endcaps (VXEC) distributed in the forward region on each side of the VXBD, as shown schematically in Figure 1. The material of each double-sided stave assumed in the simulations is $0.2\%X_0$, corresponding to $0.1\%X_0$ per layer.

The VXBD layers extend radially from 31 mm to 60 mm and have a half length of 130 mm. The VXEC layers extend in the forward direction from z=160 mm to z=257 mm and have an inner radius of 33 mm while the outer radius is 102 mm, as shown in Figure 1.

After completion of the CDR, detailed air cooling studies [2] for the vertex detector region led to a "petal" design for the VXEC planes: Sensor are arranged in sectors, azimuthally staggered with spaces large enough to allow an air flow into the VXBD region. This updated layout of the VXEC is used in the mechanical design study presented here.

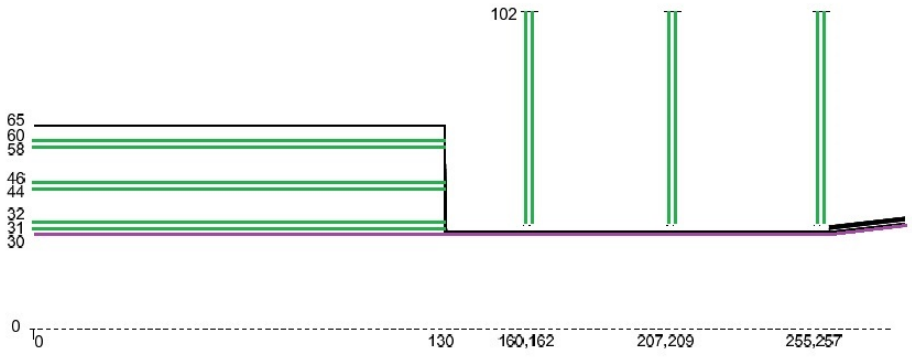


Figure 1: Schematic layout as presented in the CDR, showing the positions of the vertex detector barrel and forward layers (dimensions in millimetres). The beam pipe is shown at R=30 mm. At R=65 mm, a "barrel support shell", part of the CLIC_ILD detector model in the CDR, is indicated. For further details, see [3].

The silicon inner tracker region of the CLIC_ILD detector concept is composed of two nearly cylindrical concentric layers in the barrel region (SIT1 and SIT2 for the inner and outer one, respectively) and five forward tracking disks (FTD) in the forward region. These layers will use silicon micro-strip technology with the exception of the innermost FTD which uses silicon pixels. Figure 2 shows the schematic layout of the CLIC_ILD inner and forward tracking system.

The sub-detectors in the innermost region are supported by

- the Main Support Cylinder (directly supports the SIT2, the beam pipe, the conical shields and indirectly all the support structures listed below);
- the Outer Support Structure (directly supports SIT1);
- the Inner Support Structure (links to the vertex detector Barrel Supports and Petal Supports);
- the Petal Supports for the forward petals of the vertex detector;
- the Barrel Supports for the vertex barrel sensors.

All these CFRP structures are described in detail below, together with the Conical Shields and their support collars, as well as the cylindrical and conical sections of the beam pipe. An additional CFRP cylinder is needed to optimise the air flow for cooling the outermost vertex barrel layer - this item is called "Air-Flow Guiding Cylinder". An overview of the current engineering model is presented in Figure 3.

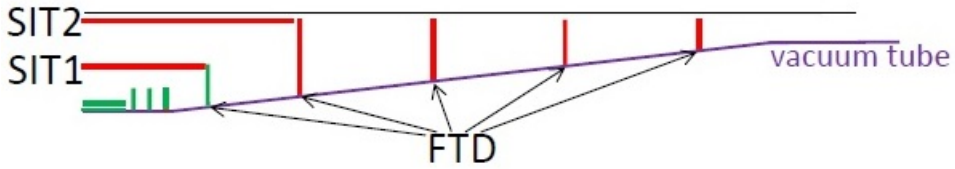


Figure 2: Schematic layout of a quarter of the CLIC_ILD inner and forward tracking system where the layers coloured in red will use silicon micro-strip technology and the remaining ones, coloured in green, silicon pixel technology. The interaction point is located near the bottom-left corner.

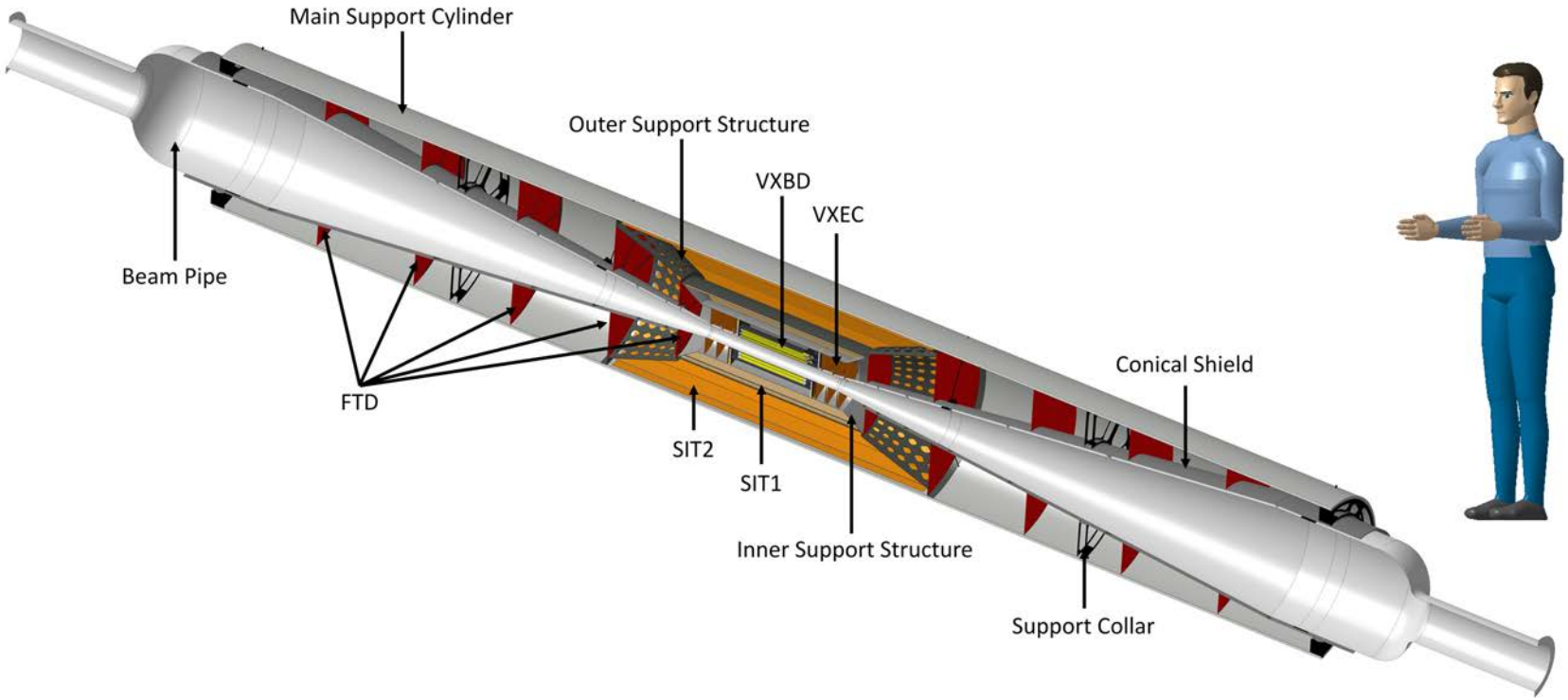


Figure 3: Section view of the engineering model for the innermost region of the CLIC_ILD detector concept. Shown are the different layers that compose the vertex detector and inner tracking system, as well as the beam pipe with the surrounding conical steel shields. The main CFRP structures required to support the detectors and the beam pipe are also shown. For reference, note that the Main Support Cylinder has an overall length of 4600 mm and an outer diameter of 664 mm.

## 2.2 Support Structures

The next subsections introduce the different CFRP support structures in the innermost region of the CLIC_ILD detector concept. The proposed designs are very preliminary, pending the evolution of the detailed detector layout, driven in turn by physics requirements and sensor technology decisions. Moreover, at this early design stage we do not elaborate on details of the mechanical connection (bolts etc.) between the different support structures.

Due to the assembly strategy, all of the major support structures are proposed to be built as two halves, This will allow to prepare the lower and upper half of the inner region to be pre-assembled and cabled separately, before joining them in a last assembly step (see section 3).

### 2.2.1 Main Support Cylinder

The CFRP Main Support Cylinder provides the mechanical stiffness and the positioning for all the detectors in the inner region as well as the beam pipe, and it directly supports the elements of SIT2. It is divided in two halves, each made of a sandwich of two skins of CFRP and a Rohacell core, with a total length of 4600 mm, an internal radius of 320 mm and a thickness of 12 mm. The layout of the different layers is shown in Figure 4. Non-symmetric deformations due to the temperature, moisture and some mechanical loads can be minimised with a symmetric layout of the CFRP layers with respect to the Rohacell core.

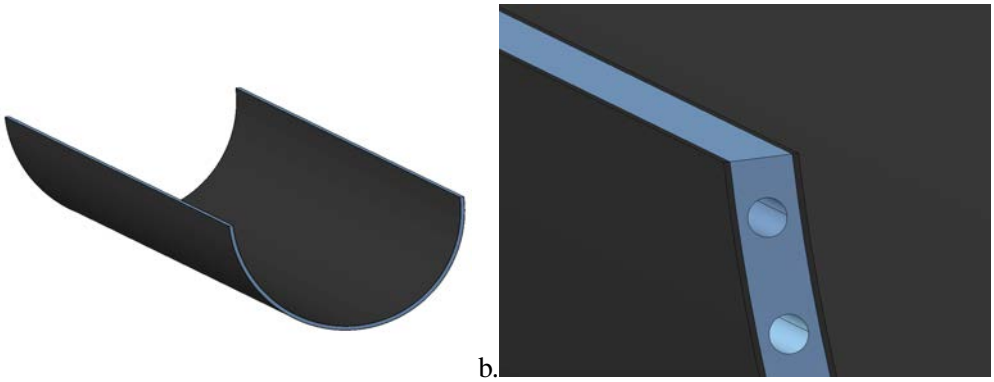

a. b.

Figure 4: a) One half of the Main Support Cylinder (total length 4600 mm); b) detail of the sandwich layout with the Rohacell core (shown in blue) between the two skins of CFRP. A possible implementation of the air cooling supply channels is also shown.

The CFRP skins in the support cylinder give the strength to the structure while the Rohacell core separates the CFRP layers in order to increase the cross-section second moment of area and bear the shear stresses. Rohacell is a low density structural foam material that allows for high strength and stiff structural sandwiches without increasing significantly their weight and the material budget. Furthermore, if needed, internal channels to supply the cooling air to the FTD layers can be easily manufactured due to the excellent machinability of Rohacell (Figure 4b).

### 2.2.2 Outer Support Structure

The purpose of the Outer Support Structure, shown in Figure 5, is to support and position SIT1, and to connect the Inner Support Structure described in section 2.2.3 to the Main Support Cylinder. This structure is made of CFRP and has a pattern of holes in its conical portions in order to allow the flow of

cooling air to the SIT1 and SIT2 layers while minimizing material at the same time. The final arrangement of holes has to be defined to avoid interference with the cabling layout in this region. A cylindrical element connects the two conical portions of the Outer Support Structure in order to increase its stiffness. This structure, split in two halves as all the symmetric support structures, is mechanically connected to the Main Support Cylinder along the outer edges of the conical portions. The total length of the Outer Support Structure is 1380 mm while the outer and inner radii are 320 mm and 168 mm, respectively. The length of the central cylindrical portion is 764 mm and the overall thickness of the structure is 0.96 mm[1].

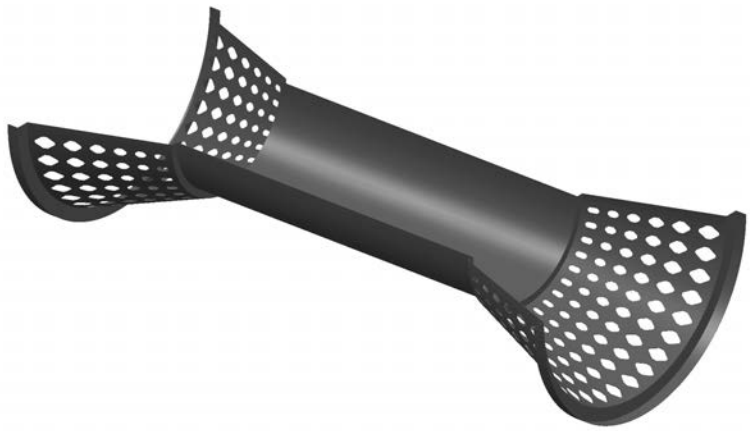

Figure 5: One half of the Outer Support Structure (total length 1380 mm).

### 2.2.3 Inner Support Structure

The Inner Support Structure, shown in Figure 6, supports the SIT1 and the CFRP supports of the vertex detector. The design of this structure follows the same principle as the Outer Support Structure: a cylindrical structure connects two CFRP cones for increased stiffness with the set being split in two parts (for assembly purposes) along the same plane as the Main Support Cylinder. It is located inside the Outer Support Structure to which it is mechanically attached along the outer edges of the two conical portions.

The total length of this structure is 765 mm and it has outer and inner radii of 176 mm and 105 mm, respectively. The total length of the central cylinder is 604 mm and the thickness of the structure is 0.80 mm.

### 2.2.4 Petal Supports

The VXEC, arranged in double-layer petals to allow air flow to the VXBD, are supported and positioned by the CFRP petal supports. Each Petal Support, shown in Figure 7a, has a detector layer on both sides and is supported by the Inner support Structure along the outer edge of the CFRP petal supports. All the petals are connected between them through a very thin CFRP cylinder on their inner edge in order to improve the mechanical robustness to air induced vibrations. A schematic CAD model with the petals attached to the thin CFRP cylinder is shown in Figure 7b.

[1] This thickness is the result of present assumptions on the details of the layered CFRP structure

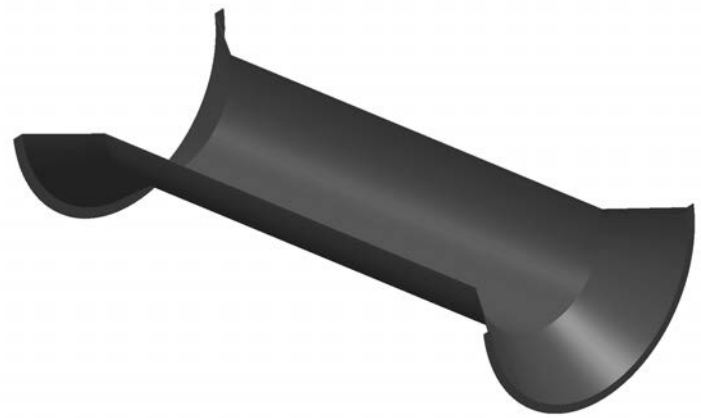

Figure 6: One half of the Inner Support Structure (total length 765 mm).

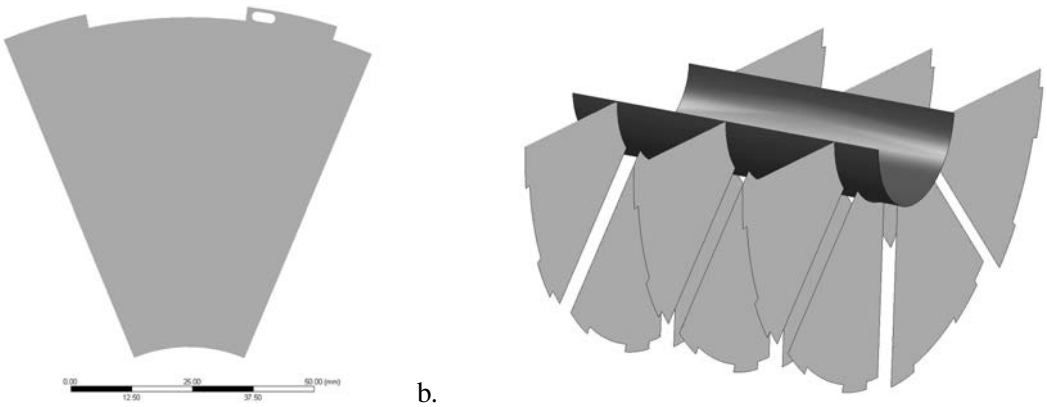

a. b.

Figure 7: a) Illustration of an individual Petal Support; b) Overview of the petals arranged in a helical pattern and connected to each other by a CFRP cylinder.

The current design for the Petal Support is the following: the angle between the radial edges is 45°, the inner radius 31 mm and the outer radius 105 mm. The petal, a sandwich of CFRP and Rohacell, has a thickness[2] of 1.74 mm. There is a longitudinal and a rotational offset of 6 mm and 45°, respectively, along the detector symmetry axis (z-axis) between a petal and the nearest one. This creates a *discrete* helical geometry, as Figure 8 shows, that is intended to be compatible with the cooling air flow.

To allow the routing of cables through the petal supports, cut-outs of different sizes on the outer perimeter are foreseen. Their dimensions vary between 10.5 mm x 3 mm and 33.5 mm x 3 mm because, depending on the petal's position in $\phi$, there are more or fewer cables which pass through it (as shown in Figure 9).

### 2.2.5 Barrel Support

The two CFRP Barrel Supports (i.e. upstream and downstream supports) support the VXBD staves and position them. Additionally, their continuous helical shape guides the air from the VXEC region to the

[2]This thickness is composed of a 120 $\mu$m thick layer of CFRP on each side of a 1.5 mm thick layer of Rohacell.

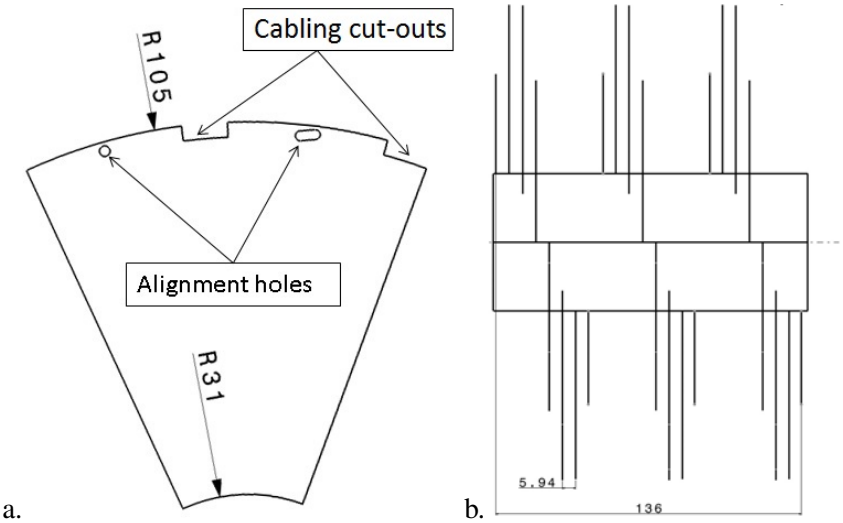


Figure 8: a) Individual Petal Support and its main dimensions; the Petal Support includes openings used to position it and cut-outs to route services through it. b) Helical layout of the VXEC showing the offset between the different petals and the distance between the innermost and outermost layer (dimensions in millimetres).

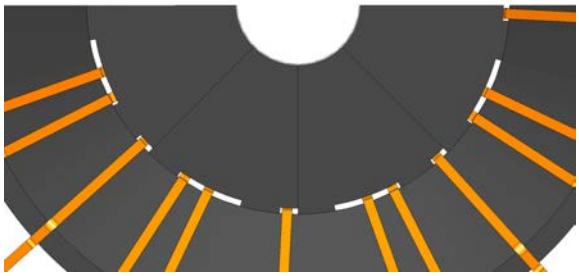

Figure 9: Front view of the Petal Supports inside the Inner Support Structure. Cables, shown in orange, cross the structures through the cut-outs on the petals.

VXBD, decreasing the flow's cross-section and hence increasing the flow speed, while maintaining the rotational momentum of the flow in order to efficiently cool all the layers of the VXBD[2]. A schematic view of the Barrel Supports is shown in Figure 10.

For assembly purposes, a Barrel Support is made of 4 different concentric modules, with the three inner ones serving as a support for the VXBD staves and the outermost one connecting them to the Inner Support Structure presented in section 2.2.3. The outermost modules on each side of the VXBD are connected by means of the CFRP Air-Flow Guiding Cylinder described in section 2.2.6. The assembly of the different modules is detailed in section 3.1. The composition of the Barrel Supports is described in Table 2 of Appendix A.

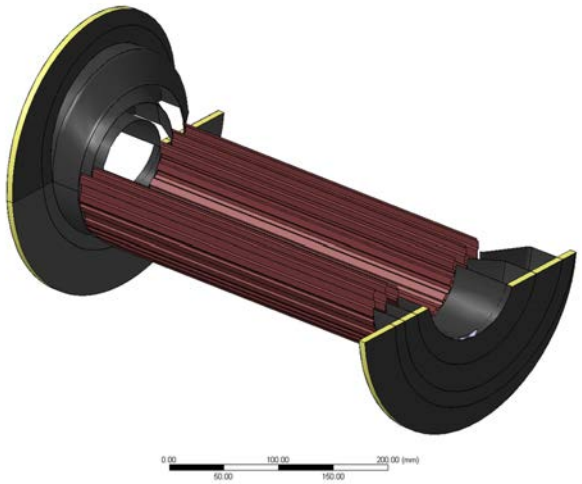

Figure 10: Schematic view of the Barrel Supports. Coloured in black are the Barrel Supports (one portion is hidden for clarity) and, in dark red, half of the support structures of the VXBD staves.

### 2.2.6 Air-Flow Guiding Cylinder

Detailed air-cooling simulations [2] suggest that an additional CFRP cylinder needs to be placed around the outermost vertex detector barrel layer, VXBD-6. This is necessary to reduce the annular opening and, in turn, increase the velocity of air-flow and the effective cooling. This Air-Flow Guiding Cylinder is suggested to have an inner radius of 71.5 mm, reducing the gap for the air-flow from 45 to 10.5 mm, as shown in Figure 11. It is expected that the insertion of this cylinder will allow sufficient cooling for VXBD-6. Detailed simulations for this scenario are, however, still pending.

a. 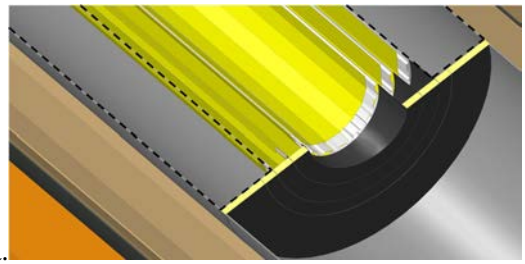 b. 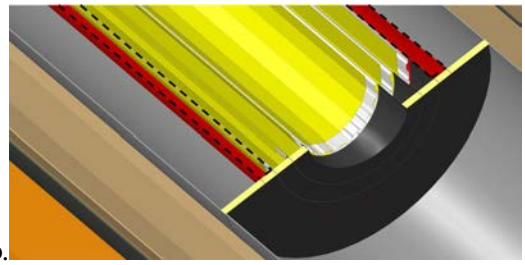

Figure 11: Air gaps between the VXVD-6 and the closest wall: a) The original design with the Inner Support Structure, leaving a gap of 45 mm to the VXVD-6 which results in low air velocity. b) The modified version with the addition of an Air-Flow Guiding Cylinder at a distance of 10.5 mm to the VXVD-6. This version is expected to significantly improve the air cooling of VXVD-6.

## 2.3 Beam pipe and Conical Shields

The central part of the beam pipe has two main elements (see Figure 3):

- a thin-walled beryllium cylinder (surrounded by the vertex detector);
- stainless steel conical parts on either side of the cylinder.

At the extremity of each conical portion, two flanges are used to connect the beam pipe to the accelerator vacuum system. The engineering details of joining the fragile beryllium cylinder to the heavy steel cones remain to be studied. A scenario for the assembly of the beam pipe inside the Main Support Cylinder is described in section 3.

### 2.3.1 Beam Pipe Design

The design of the beam pipe needs to take into consideration the following constraints [1, 4]:

1) avoiding the high rates of backgrounds from the incoherent electron-positron pairs produced in beam-beam interactions, coupled with deflection in the magnetic field. The background hit densities determine the minimum radius of the beam pipe;

2) limiting the material of the central beam pipe to $X < 0.2\%X_0$. The material budget will be discussed in more detail in Appendix C;

3) shielding against low energy background particles back-scattered from elements in the forward detector region;

4) withstanding the loads induced by the vacuum and the loads transmitted from the conical portions to the beryllium cylinder, with a safety factor of 4 to 6.

As a result of the first three constraints above, in the CDR design the beryllium cylinder has an inner radius of 29.4 mm, a thickness of 0.6 mm and a half length of 260 mm, and the beam pipe conical sections have an opening angle of 7°. The beryllium portion minimises the material inside the vertex detector, while the stainless steel conical portions provide shielding against backscattered particles. In the physics simulations, the stainless steel cones are assumed to have a wall thickness of 4 mm. However, the air cooling strategy for the inner region requires a double-walled structure to channel the air to the innermost region. The present proposal is, therefore, to have 1 mm wall thickness for the conical steel parts of the beam pipe and to add separate conical shields of 3 mm thickness at a distance of 10 mm from the beam pipe. In this gap, the air is guided by helical shaped deflectors, as shown in Figure 12, that induce the rotational momentum to the flow as required by the cooling strategy. Introducing this 10 mm gap decreases the forward angular acceptance from 7 to 8.3 degrees.

The cooling strategy currently being studied does not foresee the conical shield to extend along the full length of the conical portion of the beam pipe towards the central region (see Figure 12). If required for shielding purposes, the extension of the conical shield towards the IP will result in a more significant reduction in acceptance, from 7 to 9.1 degrees.

### 2.3.2 Beam Pipe Supports

As shown in Figure 13, the beam pipe is supported by two collars on each stainless steel cone, at a distance to the IP of 700 mm for the inner collar and 2200 mm for the outer one. Each of the inner collars

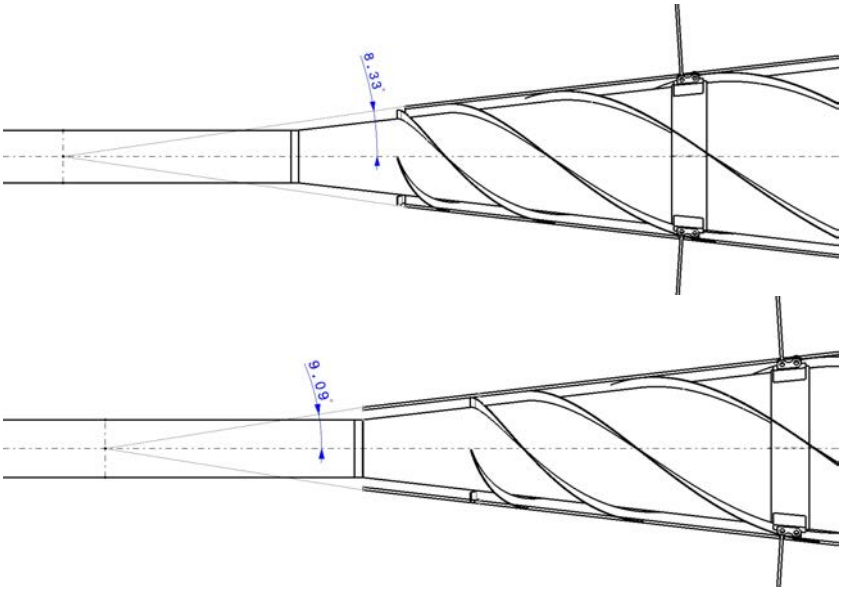


Figure 12: (Top) Sketch showing the limiting angle of 8.3 degrees for the forward acceptance in the current engineering model. (Bottom) The reduced acceptance (9.1 degrees) in case the conical shield is extended towards the interaction point. The spiralling air flow deflectors placed around the conical part of the beam pipe are also indicated.

is connected to three radial spokes that transfer the vertical loads of the beam pipe to the Main Support Cylinder, traversing the 3 mm thick stainless steel conical shields. The outer collars are connected to the Main Support Cylinder by means of six spokes. Three of these spokes are placed in the radial direction and also transfer the vertical loads.

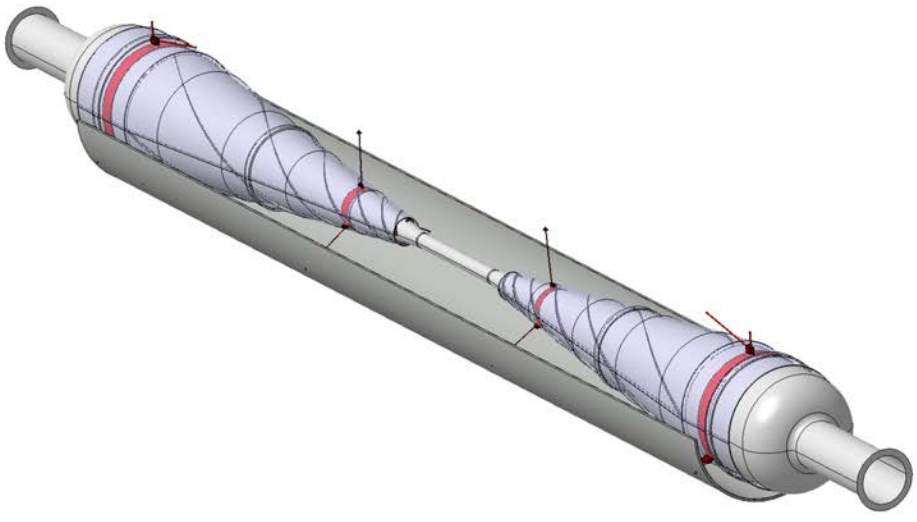

Figure 13: One half of the Main Support Cylinder connected to the beam pipe through 18 spokes. The spokes have to go through the stainless steel conical shields (purple colour) that surround the beam pipe.

### 2.3.3 Support Collars for Conical Shields

The conical shield support collars are CFRP structures that surround the stainless steel conical shields described above. As Figure 14 shows, they are semicircular structures located in the forward region (i.e. in the FTD region) which support each conical shield in two locations from the Main Support Cylinder. In total, four pairs of collars are needed.

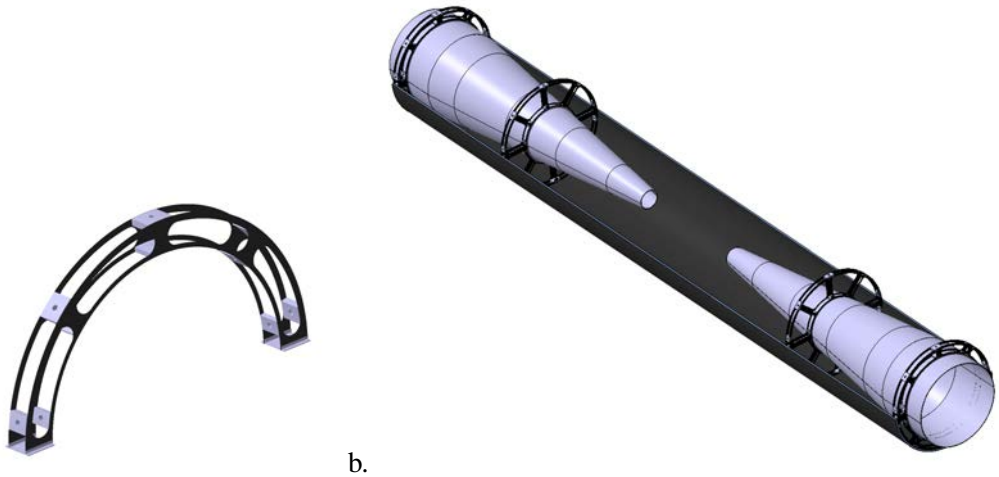

a. b.

Figure 14: a) A semicircular collar to fix the steel Conical Shield to the Main Support Cylinder; b) the proposed location of the four pairs of support collars.

# 3 Assembly Process

The assembly procedure of the detectors and corresponding support structures involves three separate sub-assemblies: (1) contains the vertex detector and the SIT1 and SIT2 layers (top and bottom half); (2) concerns the beam pipe and its support spokes; (3) comprises the FTD and the steel Conical Shield (top and bottom half). These sub-assemblies can be prepared separately, before the final overall assembly. The proposed assembly sequences are presented in the following sections.

## 3.1 Sub-assembly of the vertex detector and inner tracking layers

This sub-assembly is shown in Figure 15. The sequence starts with one half of the Main Support Cylinder being placed on a structure dedicated to this sub-assembly. Then, the staves forming SIT2 are inserted and their services routed. The next step is the installation of the Outer Support Structure, the SIT1 staves and their service. Following this, the Inner Support Structure can be inserted.

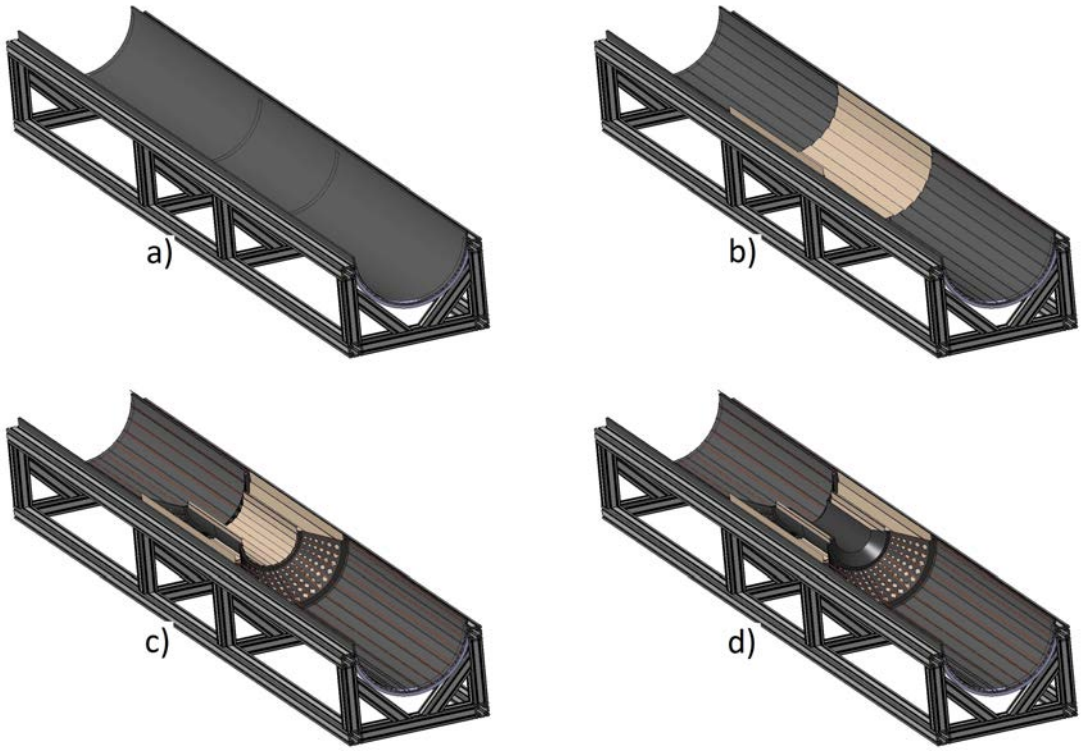


Figure 15: Sub-assembly of the vertex detector and inner tracking layers: a) half of the Main Support Cylinder placed on a dedicated structure; b) SIT2 staves and their services in their final position inside the Main Support Cylinder; c) the Outer Support Structure inserted, along with the SIT1 staves and their services; d) the Inner Support Structure in place.

Once the Inner Support Structure is in place, the vertex detector can be inserted. Its different steps are shown in Figure 16. First, the Air-Flow Guiding Cylinder is inserted along with the supports of the outermost VXBD layer. Next, the outermost VXBD layer and its cables are inserted, followed by the supports, staves and cables of the middle VXBD layer. Finally, the same procedure is repeated for the innermost VXBD layer. The final step is the insertion of each VXEC petal and its services, starting from the innermost one and going through each petal following their relative placement in the z-direction. The assembled petals are shown in the bottom right of Figure 16.

The completed sub-assembly of one half of the vertex detector and inner tracking layers is shown in

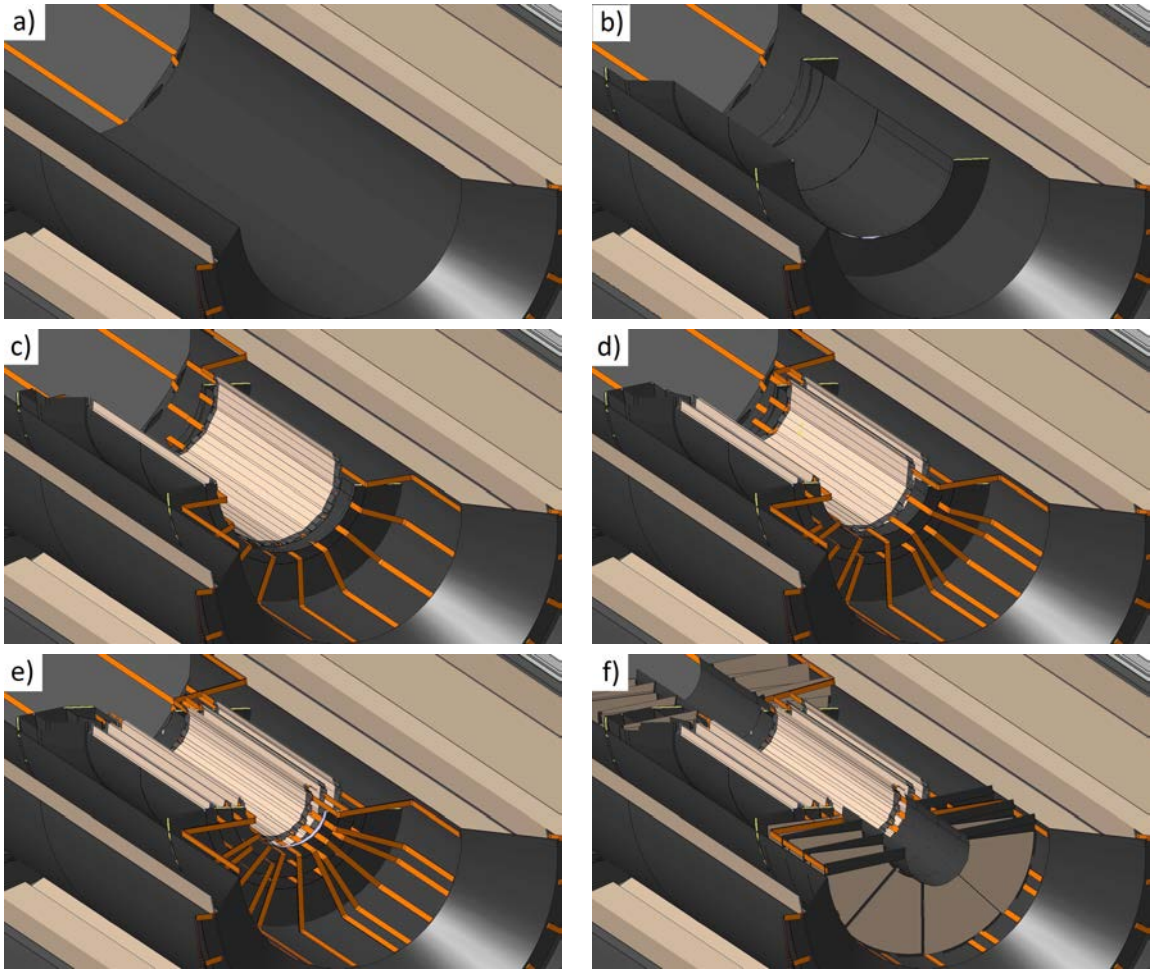


Figure 16: Sub-assembly of the vertex detector and inner tracking layers: a) detailed view of the Inner Support Structure in its final location; b) Air-Flow Guiding Cylinder and outermost VXBD layer supports once assembled; c) detailed view of the outermost VXBD layer in place with its services; d) middle VXBD layer in place with its services; e) detailed view of the innermost VXBD layer in place with its services completing the assembly of the vertex detector barrel; f) VXEC petals assembled inside the inner region (their services follow the same path as the ones of the VXBD).

Figure 17. The procedure described above is repeated for the other half of the innermost region of the detector.

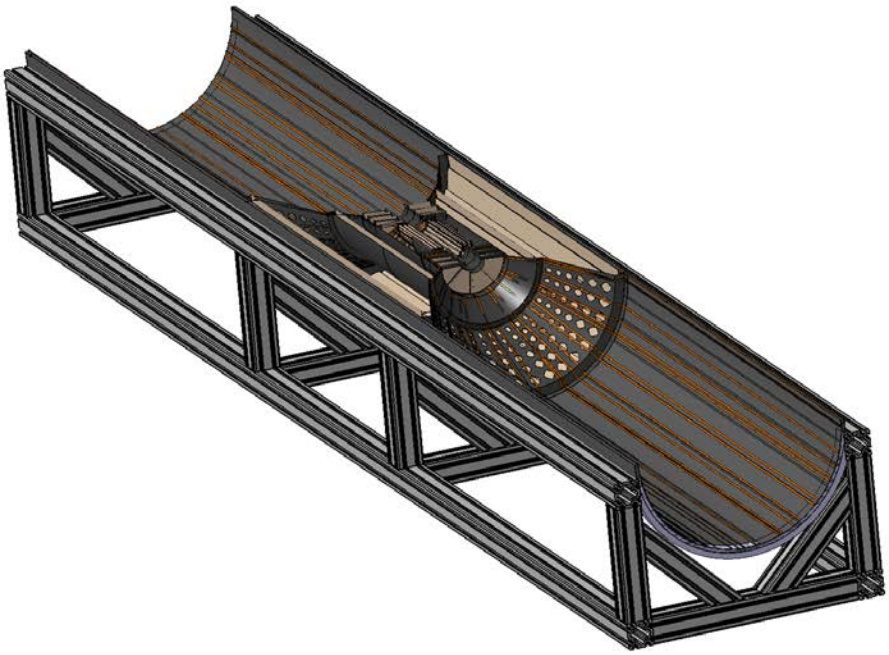

Figure 17: The sub-assembly of the vertex detector and inner tracking layers. Two of these sub-assemblies will be prepared separately.

### 3.2 Sub-assembly of the beam pipe

As discussed in Section 2.3.1, the beam pipe is composed of a central beryllium cylinder and two stainless steel cones in each side of it. The beam pipe is supported from the Main Support Cylinder by a system of collars and spokes (see Figure 13). The preparation of the beam pipe for the final assembly process is shown in Figure 18.

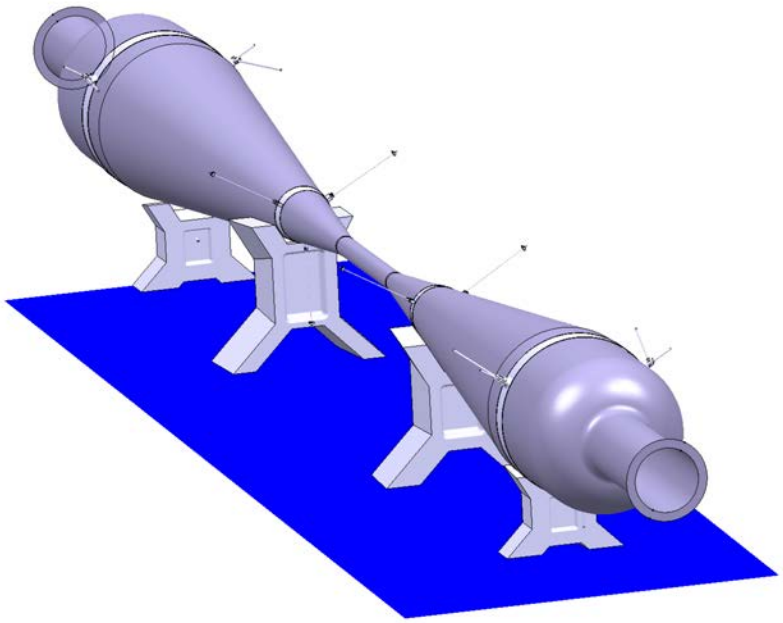

Figure 18: Preparation of the beam pipe for the final assembly of the inner region. With the beam pipe resting on temporary supports, the four collars and their 18 support spokes are added to it.

### 3.3 Sub-assembly of the FTD and steel Conical Shields

In addition to their shielding function, the two steel cones will also serve as support for the FTD and their cables. Using a dedicated temporary support, shown in Figure 19a, two half Conical Shields are supported from their inner surfaces while the FTDs are placed on their outer surfaces. Once the innermost disk (FTD-1) is in place and its cables routed along the stainless steel shield (Figure 19b), the procedure is repeated for the next disks until the outermost disk (FTD-5) is in place, as shown in Figure 19. Finally, once all the FTDs are placed, the support collars that connect the Conical Shields to the Main Support Cylinder are attached to the shields, as the bottom right part of Figure 19d shows.

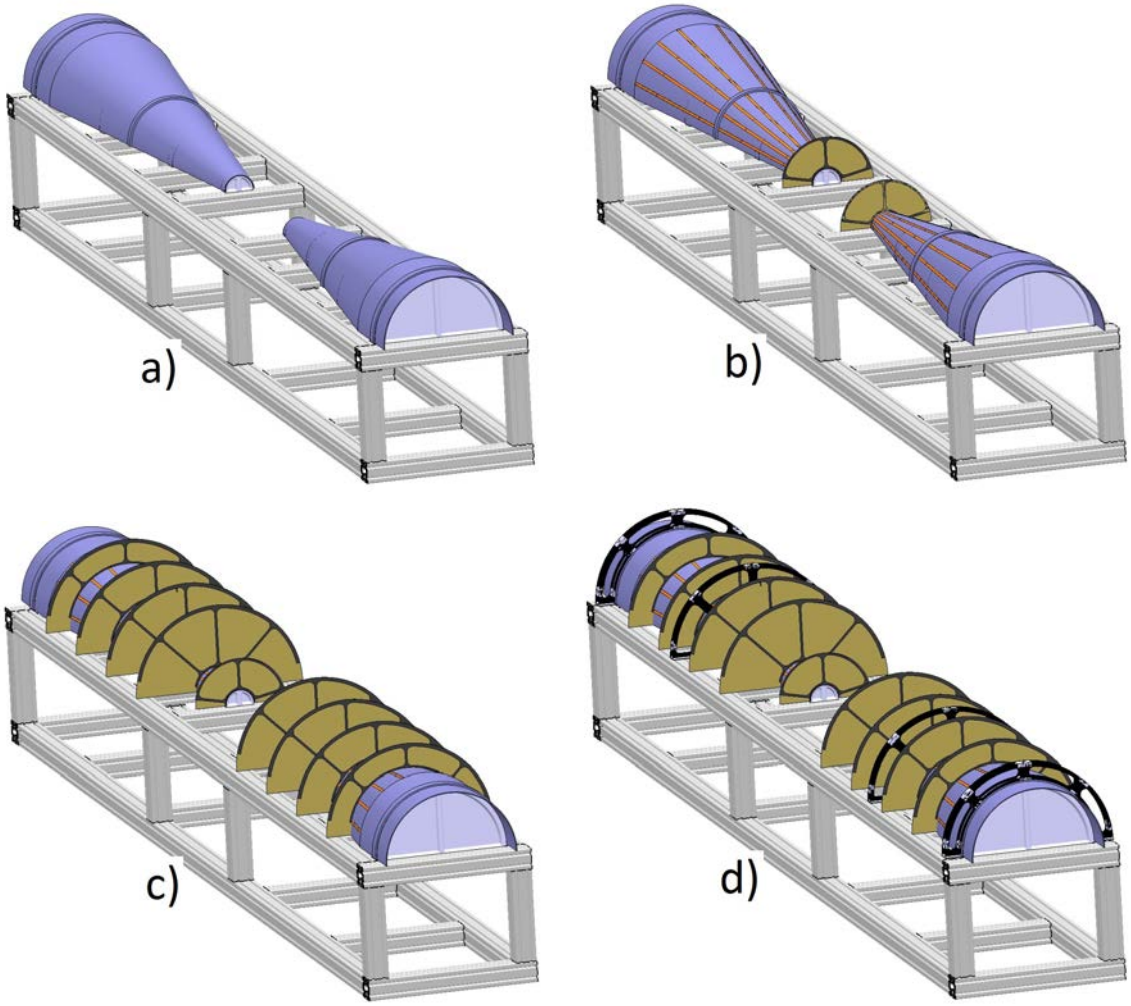


Figure 19: Sub-assembly of the FTDs and stainless steel Conical Shields: a) two half Conical Shields on a dedicated temporary support; b) assembly starts with the placement of the innermost FTD disks and their cables; c) the disks and their services are placed sequentially from the innermost to the outermost; d) once all the disks are in place, the support collars are attached to the Conical Shields.

### 3.4 Final assembly

Once the sub-assemblies described in the previous sections are ready, the final assembly starts by lifting one of the two sub-assemblies of the vertex detector and inner tracking layers (see Figure 17) and rotating it by 180° along the z-axis. Subsequently, it is lowered onto one of the sub-assemblies of the FTD and Conical Shields, as shown in Figure 20a. Once in contact, both sub-assemblies are connected along the outer edge of the support collars. Then, the assembly is lifted onto the beam pipe, as shown in Figure 20b. The upper beam pipe support spokes can then be connected to the Main Support Cylinder. Once done, the beam pipe supports can be removed.

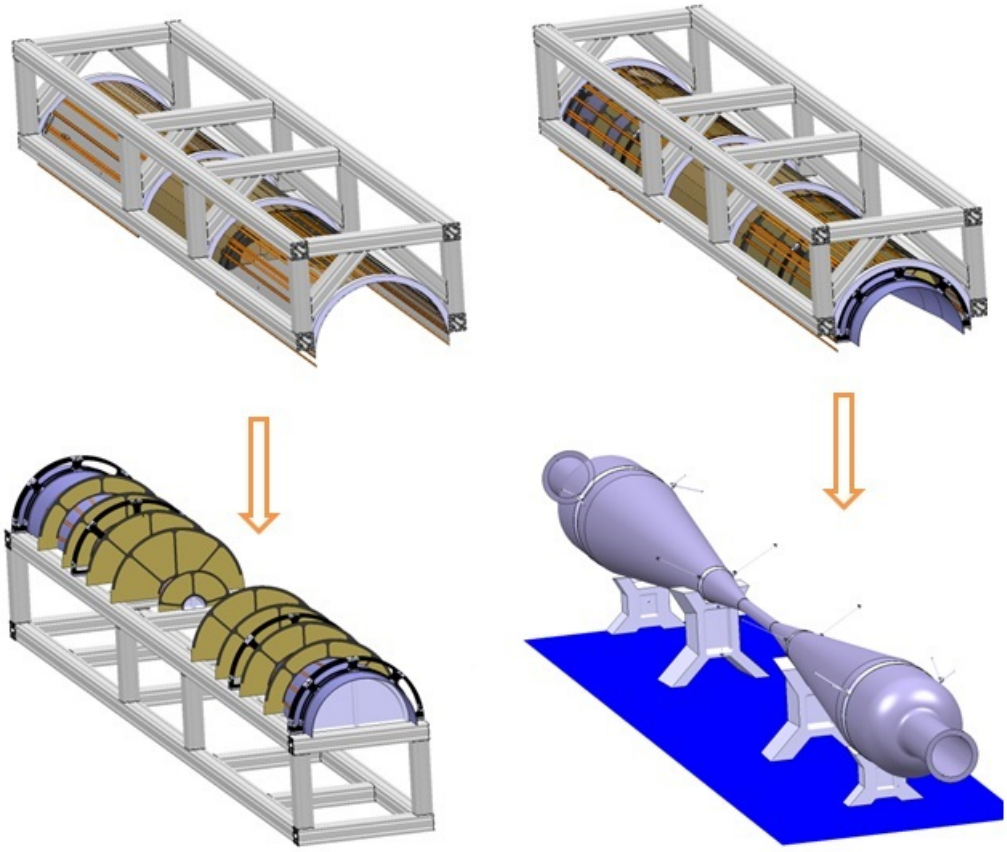

a. b.

Figure 20: Final assembly part 1: a) one of the sub-assemblies of the vertex detector and inner tracking layers is lowered onto, and connected to, a sub-assembly of the FTD and Conical Shields; b) this assembly is then lowered onto the beam pipe and its upper support spokes are connected to the Main Support Cylinder.

This upper-half assembly plus beam-pipe is then lowered onto the second sub-assembly of the FTD and Conical Shields and connected to it along the radial edges of the support collars (Figure 21a). The assembly can then be lifted and positioned onto the second sub-assembly of the vertex detector and inner tracking layers, as shown in Figure 21b. The lower beam pipe support spokes are attached to the Main Support Cylinder. Finally, both half-assemblies are connected at each other along the outer edges of the support collars and the longitudinal edges of the Main Support Cylinder, forming a inner detector module that can be inserted as a whole (inside the TPC, in case of the CLIC_ILD concept).

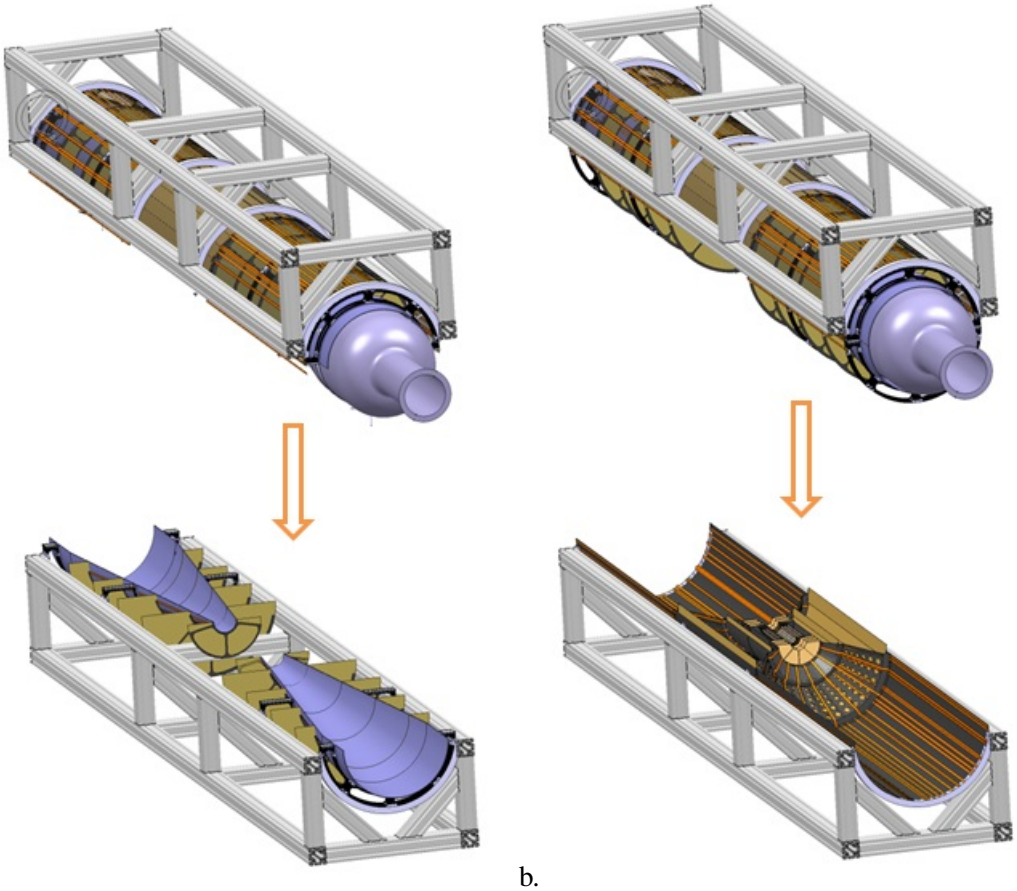

a. b.

Figure 21: Final assembly part 2: a) the partial assembly is lowered onto the remaining sub-assembly of the FTD and conical shields and attached to it along the radial edges of the support collars; b) the resulting structure is then lowered onto the remaining sub-assembly of the vertex detector and inner tracking layers and connected to it along the outer edges of the support collars and the longitudinal edges of the Main Support Cylinder, while the lower beam pipe support spokes are attached to the Main Support Cylinder.

# 4 Conclusions

This technical note has introduced a possible scenario for the layout and assembly process of the inner region of a CLIC detector (using the layout of CLIC_ILD as a basis). A design for some of the support structures is proposed, which tries to minimise the static deformations due to the weight of the different components and dynamic deformations due to the vibrations produced by air cooling.

A preliminary design of the beam pipe and its supports has been presented, and the results from analytical and numerical calculations are appended. These results indicate that buckling will occur if the beam pipe stainless steel cones are only 1 mm thick. While some solutions to this problem are proposed, further studies are needed. Other detailed design studies for a number of mechanical components, most importantly for the systems needed to join (bolt together) the sub-assemblies, are still missing.

With the definition of the different components, the material budget in the engineering model has been calculated and compared to the values presented in the CDR. The calculated values are near the ones proposed as a realistic target in the CDR. An optimisation of the mechanical design, in order to further reduce the material budget, can be envisaged at a later stage of the CLIC detector design.

# 5 Appendix A: Numerical Simulations of the CFRP Support Structures

## 5.1 Introduction

Simulations are needed in order to verify the choice of materials and the concept chosen in the design of the CFRP structures. However, given the early stage of the design, only preliminary simulations are possible since many details are still missing (e.g. material budget, maximum deformations and required stiffness, design of the mechanical joints, etc.). A second observation to be made is that the structures have not yet been fully optimised in their design due the ongoing parallel work on the sensors design, air cooling and cabling layout which requires a constant updating of the support structures. For this reason, the results shown below must be considered as qualitative and used only as a guideline for the subsequent stages of the design.

The geometrical details of each structure have been already discussed in the previous sections. For the simulation the same geometry is used. The software used to perform the simulations was ANSYS WORKBENCH v14.5.

Simulations were made for the Inner Support Structure and the components inside it. Due to the geometrical complexity, three complementary simulations have been performed:

- Simulation of the Barrel Support with its own weight and the weight of the VXBD staves (Figure 22).
- Simulation of the VXEC Petal Support with its own weight, the weight of the VXEC, a load resulting from the gradient of pressure between the two faces due to the air cooling and a gradient of temperature of 20 °C (Figure 23).
- Simulation of the remaining structure with an equivalent load corresponding to the weight of VXBD and the Barrel Support as well as the VXEC petals (Figure 24).

## 5.2 Materials and boundary conditions

The materials used in the simulation and their mechanical properties are defined in Table 1:

Table 1: Mechanical properties of the M55J CFRP UD prepreg[5] and the Rohacell [6].

| Material | Young's Modulus in the fiber direction (x) [GPa] | Young's Modulus in the transverse direction (y,z) [GPa] | Poisson's ratio xy | Density [kg/$m^3$] | Thermal expansion coefficient [$K^{-1}$] (x,y,z) directions |
|---|---|---|---|---|---|
| M55J UD | 324.4 | 5.8 | 0.208 | 1660 | (-4.5·$10^{-7}$, 3·$10^{-5}$, 3·$10^{-5}$) |
| Rohacell | 0.09 | 0.09 | 0.32 | 75 | – |

The layout of the plies in the different CFRP structures described in section 2.2 are shown in Table 2, which also presents the total thickness of each structure.

The boundary conditions applied to the CFRP structures correspond to fixed supports to the ground such that it serves as a reference for the deformations. The structures are loaded with their own weight and the weight of the detectors supported by them. The estimated mass of each double-sided VXBD detector stave is 5.6 g while the value estimated for the VXEC detector petals (assumed proportional to the mass of the VXBD detector on an area base) is 5.2 g. Furthermore, for the simulation of the VXEC Petal Support, two additional loads were considered: due to the flow of air, there is a difference of pressure between the two sides of each petal which, based on preliminary CFD simulations, has been estimated to result in a load that has a maximum value of 0.5 N; and, due to the heating of the sensors, a gradient of 20°C has been considered.

Table 2: Layout of the CFRP plies in the different support structures.

| Structure | Layout | Thickness [mm] |
|---|---|---|
| Main Support Cylinder | $[0.90,\overline{Rohacell}]_{TBD*}$ | 12 |
| Outer Support Structure | TBD* | TBD* |
| Inner Support Structure | $[(\pm 30)_s]_{2s}$ | 0.8 |
| Petal Support | $[0.45,\overline{Rohacell}]_s$ | 1.74 |
| Barrel Support | $[(\pm 20)_s, \overline{Rohacell}]_s$ | 5.4 |
| Air-Flow Guiding Cylinder | $[\pm 30]_s$ | 0.2 |
| Support collar | TBD* | TBD* |
| Vertex stave | $[0,\overline{90}]_s$ | 0,09 |

*remain to be defined

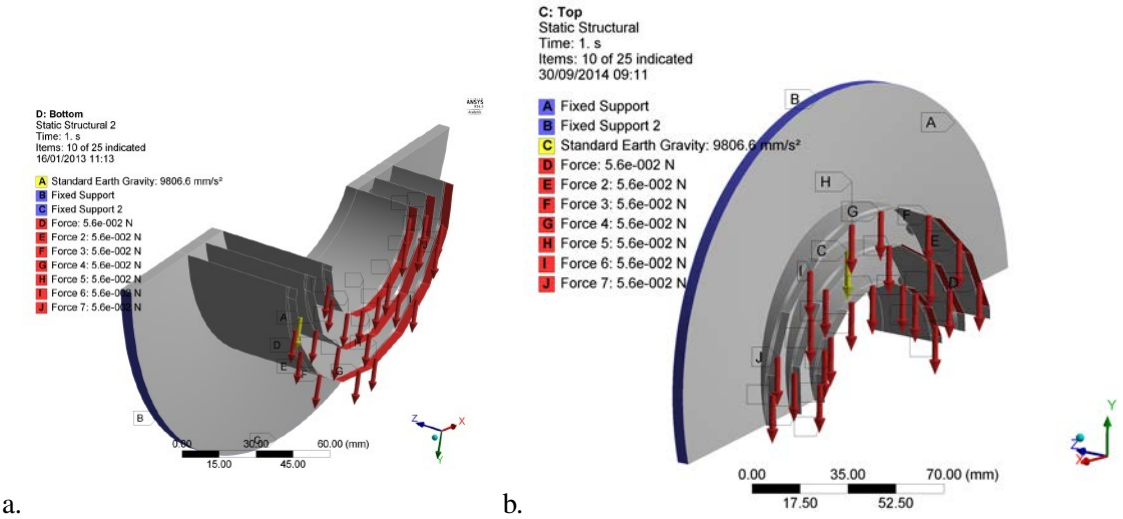


a. b.

Figure 22: Boundary conditions for the Barrel Support simulation with red arrows showing the loads corresponding to the weight of the VXBD staves and a blue surface showing the fixed support area of the structure.

## 5.3 Mesh

The structures have been meshed using quadratic (8 nodes) elements for the CFRP layers and quadratic (20 nodes) hexahedron solid elements for the Rohacell cores. The size of the elements varies between 2 mm and 7 mm. The resulting meshes are shown in Figures 25, 26 and 27.

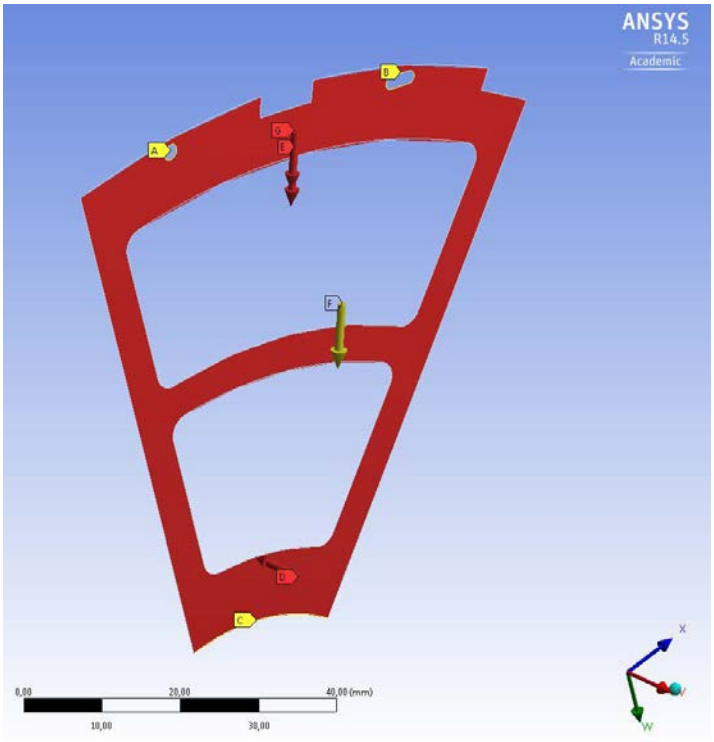


Figure 23: Boundary conditions for the VXEC Petal Support simulation with red arrows showing the different loads applied (i.e. the weight of the VXEC and force resulting from the gradient of pressures due to air cooling). The yellow arrow shows the direction of the gravitational load. The petal is supported through a clamped boundary condition in its external and internal perimeter (simulating the connection to the Inner Support Structure and the thin CFRP cylinder).

### 5.4 Simulation results

The results from the simulations are shown in Figures 28, 29 and 30. The deformations due the weight of the components are low, between 13 $\mu$m in the Petal Support and 32 $\mu$m in the barrel support. The Petal Support deformations increase to 137 $\mu$m if the load of the air is added, i.e. if a pressure gradient that results in a load of 0.5 N is assumed. Further studies must however be done to accept or reject these results as well as a modal analysis to simulate the dynamic behaviour of the structures.

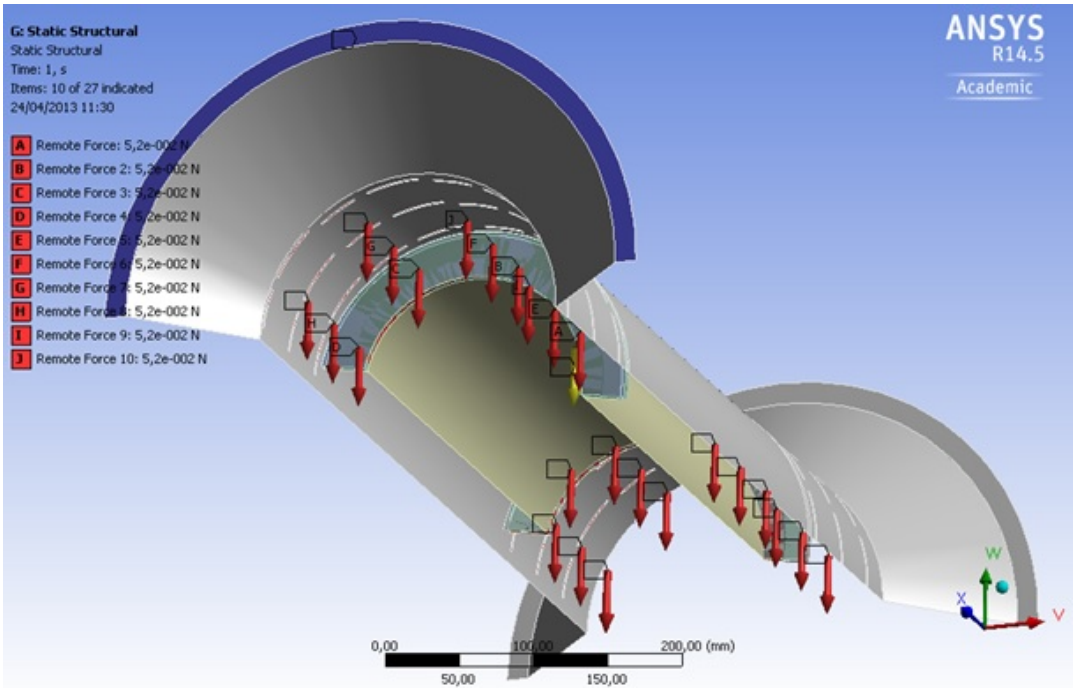


Figure 24: Boundary conditions for the Inner Support Structure simulation with the loads (shown with red arrows) of the VXEC, CFRP supports and VXBD weight. The blue surface shows the fixed support area of the structure (i.e. the connection with the Outer Support Structure) and the yellow arrow shows the direction of the gravitational load.

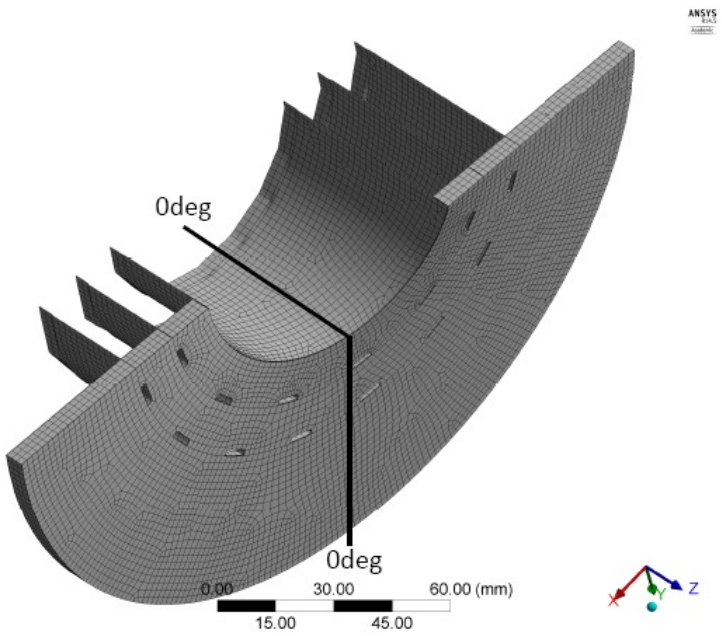


Figure 25: Mesh used for the barrel support simulation. The black solid lines indicate the angular reference of the laminate's layout.

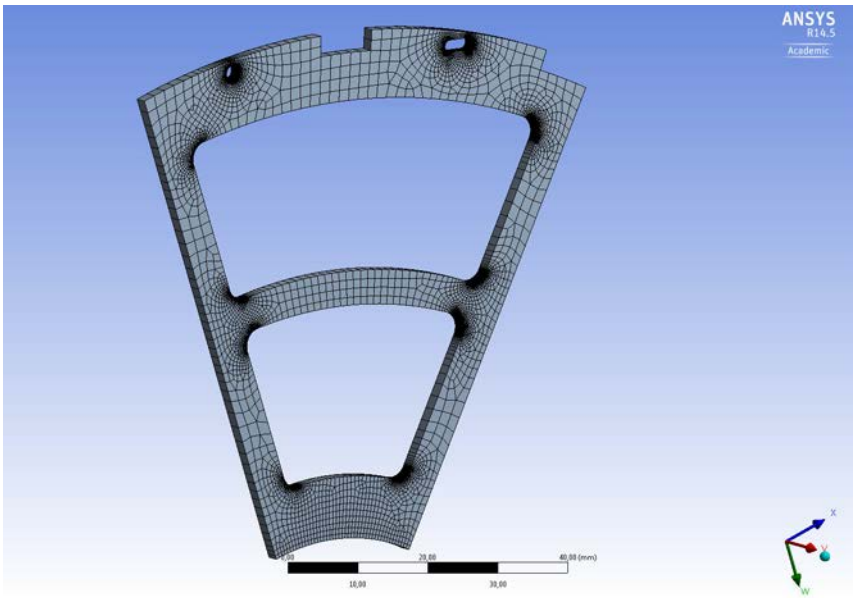


Figure 26: Mesh used for the VXEC Petal Support simulation.

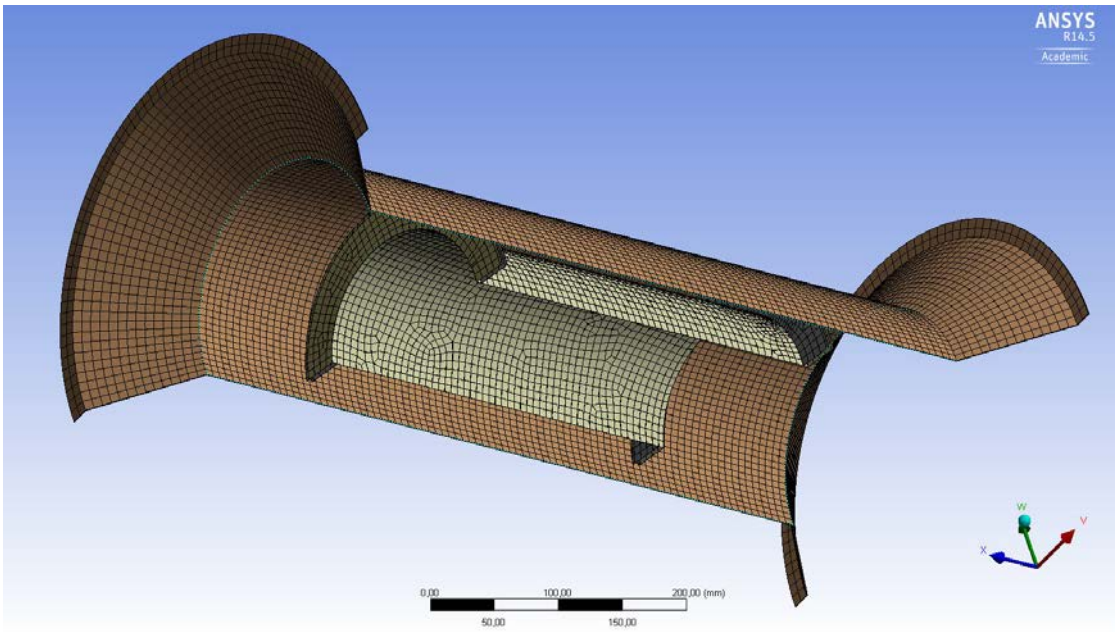


Figure 27: Mesh used for the Inner Support Structure simulation.

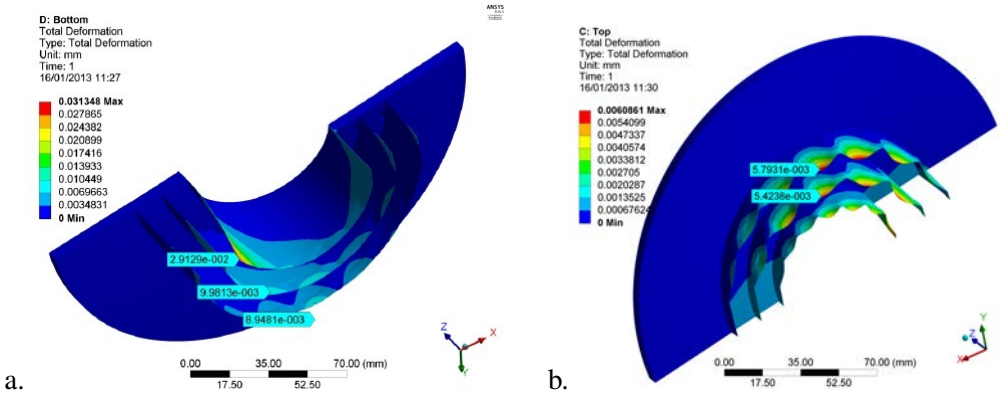


Figure 28: Results from the simulation of the Barrel Support in its two different configurations (top and bottom). The deformation due the weight of the VXBD and the structure itself is below 32 $\mu$m.

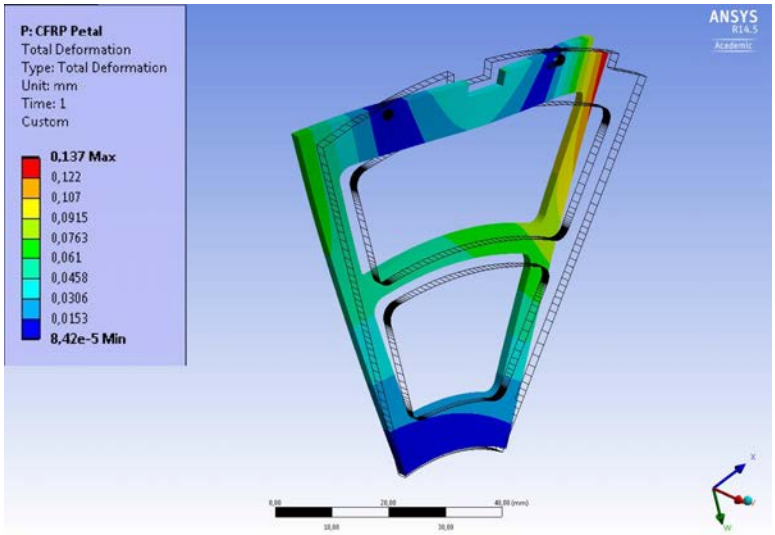


Figure 29: Results from the simulation of the Petal Support. The maximum deformation is 137 $\mu$m and is produced by the load resulting from the pressure gradient in the perpendicular direction of the CFRP petal. The effects of the weight and the thermal expansion are small compared with the effect of pressure. Reducing the size of the openings in the petal, the deformations can be minimised but at the expense of an increase of the material budget. The black lines in the picture show the undeformed shape of the petal.

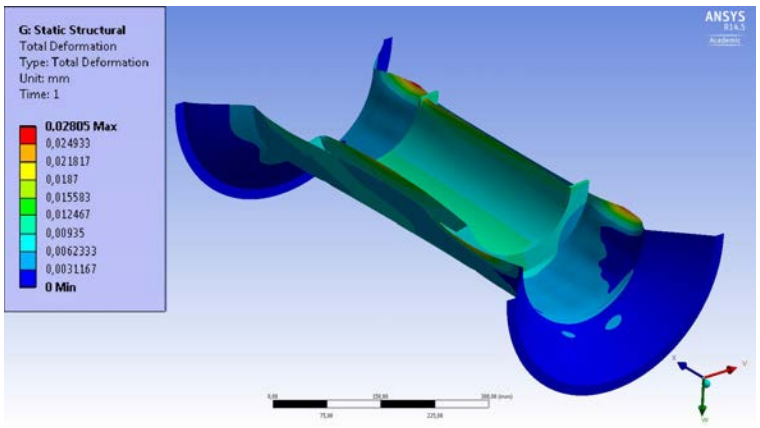


Figure 30: Results from the simulation of the Inner Support Structure. The resulting deformation is below 29 $\mu$m.

# 6 Appendix B: Beam Pipe Engineering Calculations

## 6.1 Beam pipe analytical calculations

The beam pipe's working loads required to be taken into account for its design are the following:

- The own weight of the beam pipe;
- The pressure gradient between the inside and the outside of the beam pipe ($10^5$ Pa);

Two less important loads should be mentioned, even though they are not taken into account at this stage of the design: The loads induced by the air flow that surrounds the beam pipe and the temperature gradient along the beam pipe due to both self-heating of the beam pipe and heat exchanges with the surrounding cooling air.

Engineering simulations are needed in order to check the beam pipe design against strength and buckling failure. Both analytical calculations and numerical simulations were performed. The analytical bucking calculations were done considering a truncated conical shell, with constant thickness, made of AISI 316L stainless steel under an external pressure of $10^5$ Pa. The results, based on formulas provided by different authors, are shown in Table 3.

Table 3: Analytical buckling load multipliers, based on formulas from several publications, for the beam pipe conical shell under the action of the atmospheric pressure.

| Reference document | Load multiplier |
|---|---|
| ECCS [7] | 0.46 |
| DNV-RP-C202 [8] | 0.34 |
| NASA SP-8019 [9] | 0.48 |
| Roark's formulas for stress and strain [10] | 0.66 |
| Brush and Almroth [11] | 0.81 |

Table 3 shows different values for the load multiplier (equivalent to the safety factor) depending on which reference is considered for the calculation. This is explained firstly by the underlying methods proposed in the different publications, some having a purely theoretical base while others include empirical factors. Secondly, some of the methods are more conservative than others due to the inclusion of implicit safety factors.

Despite the differences in the calculated value of the load multiplier (see Table 3), the results show that, no matter which formula is used, the conical portions of the beam pipe are expected to buckle (i.e. the load multiplier is lower than 1) under the atmospheric pressure with the current design. Furthermore, if one considers that, for these type of objects, safety factors between 4 and 6 are normally required, it is clear that the current layout does not satisfy the design requirements.

## 6.2 Beam pipe numerical calculations

Given the difficulty in obtaining accurate results using analytical methods, numerical simulations are needed in order to verify the materials and the concept chosen for the design of the beam pipe. The geometrical aspects have been discussed in the previous sections with, for the simulation, the same geometry is used. The present simulation has as a guideline other beam pipe simulations that have been performed in the past such as those for the ILD beam pipe [12].

### 6.2.1 Materials and working conditions

The materials proposed in the CDR and hence, used in the simulation, are beryllium and AISI Type 316L stainless steel, for which the mechanical properties are shown in Table 4.

Table 4: Mechanical properties of beryllium and AISI 316L stainless steel.

| Material | Young's Modulus [GPa] | Poisson's ratio | Density [kg/$m^3$] | Yield Strength [MPa] |
|---|---|---|---|---|
| AISI 316L | 193 | 0.31 | 8000 | 290 |
| Beryllium | 303 | 0.07 | 1850 | 240 |

The beam pipe is supported by 18 spokes, as described in section 3.2, connected to four collars that surround the beam pipe. To simulate the behaviour of the spokes, 18 spring elements have been added to the model. To precisely position the beam pipe, the spokes are pre-loaded in order to work under traction loads during the life cycle of the beam pipe. These loads are enumerated in Table 5, where $S_n$ corresponds to the location of the spring, as shown in Figure 31 and $L_n$ corresponds to the applied pre-load.

Table 5: Calculated pre-load for each support spring used in the simulation.

| $S_n$ | $L_n$ |
|---|---|
| $S_1$ | 45 N |
| $S_2$ | 180 N |
| $S_3$ | 300 N |

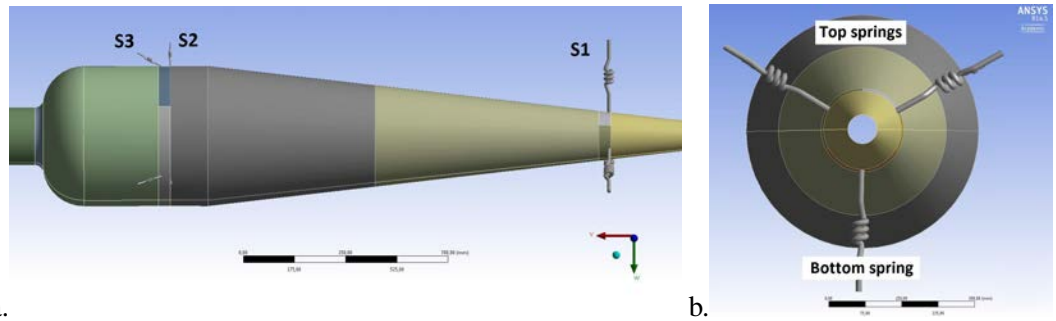


a. b.

Figure 31: Location of the springs used to simulate the 18 spokes that support the beam pipe. The springs are pre-loaded differently as a function of their position and angle.

To achieve a similar behaviour of the springs with respect to the spokes, the stiffness of the spring needs to be calculated. Hence, considering unidirectional CFRP as the spoke's material, with a Young's modulus of $E = 181$ GPa in the spokes' direction, a radius of 1 mm and applying the relation of the equation 1, it is possible to obtain the stiffness of the spring to be used in the simulation:

$$k_n = \frac{E \cdot A}{l_n} \tag{1}$$

where $k_n$ is the longitudinal stiffness of each spring, $l_n$ the length of the spring from the joint with the collar to the connection to the Main Support Cylinder, $E$ the Young's modulus in the spoke's direction

and $A$ is the spoke's cross-section area. The subscript $n$ corresponds to the different springs used to perform the simulation.

The different values of the spring's longitudinal stiffness $k$ are shown in Table 6.

Table 6: Calculated longitudinal stiffness for each spring length.

| $S_n$ | $l_n$ | $k_n$ |
|---|---|---|
| $S_1$ | 250 mm | $2.27 \cdot 10^6$ N/m |
| $S_2$ | 82 mm | $6.01 \cdot 10^6$ N/m |
| $S_3$ | 95 mm | $6.93 \cdot 10^6$ N/m |

### 6.2.2 Mesh

The beam pipe has been meshed using quadratic (8 nodes) shell elements. In total there are around 18000 elements with a size between 5 mm in the most detailed areas, such as the beryllium beam pipe, and 40 mm elsewhere, as shown in Figure 32.

a.

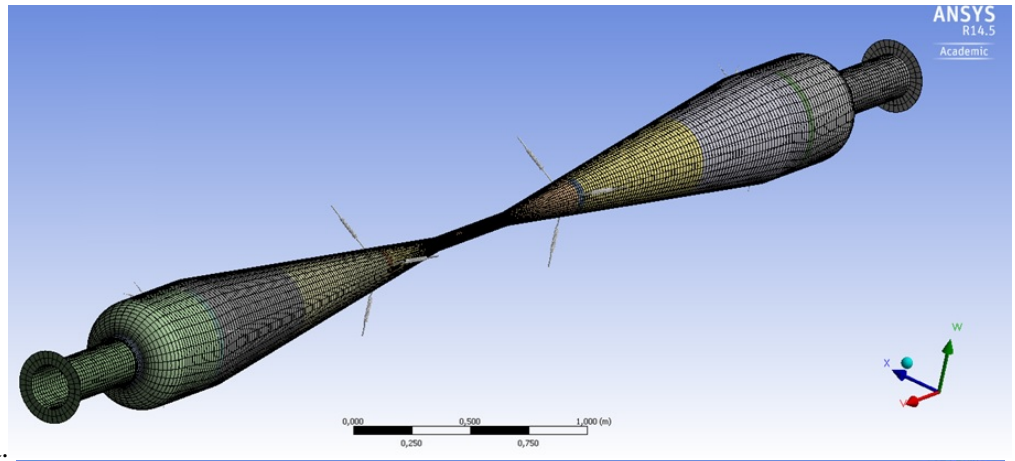


b.

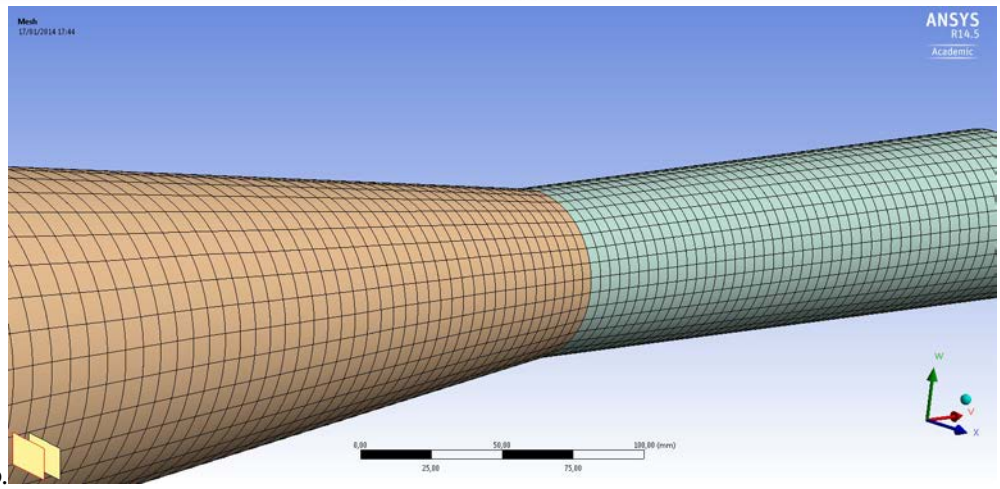


Figure 32: Mesh used in the static and linear buckling simulations of the beam pipe. a) General view of the beam pipe with the support springs and b) detail of the mesh in the transition between the beryllium cylinder and the conical stainless steel portions.

### 6.2.3 Loading Conditions

As discussed in Section 2.3.1, the loads applied in the simulation are the own weight of the beam pipe and the gradient of pressure between inside and outside. The weight of the beam pipe is approximately 23 kg and the external atmospheric pressure is $10^5$ Pa. Viscosity loads due to the air flow surrounding the beam pipe are neglected. Given the preliminary nature of this simulation, temperature gradients are also not considered. As described in section 6.2.1, a pre-load, with the values enumerated in Table 5, was applied to the support springs. In the model, one side of the springs is connected to the beam pipe. The other side of the springs is simulated as being simply supported, an approximation of the connection to the Main Support Cylinder in the real assembly. Given that the connection between the stainless steel cones and the beryllium beam pipe has not yet been studied in detail, the generated mesh imposes continuity of displacements and rotations across the joint between these two parts.

### 6.2.4 Results and Preliminary Conclusion

The results obtained from the mechanical static analysis are shown in Figures 33, 34 and 35. The maximum stress under the Von Mises criteria is 72 MPa, for the stainless steel parts, and 40 MPa for the beryllium cylinder. The values and the calculated safety factor are summarized in Table 7.

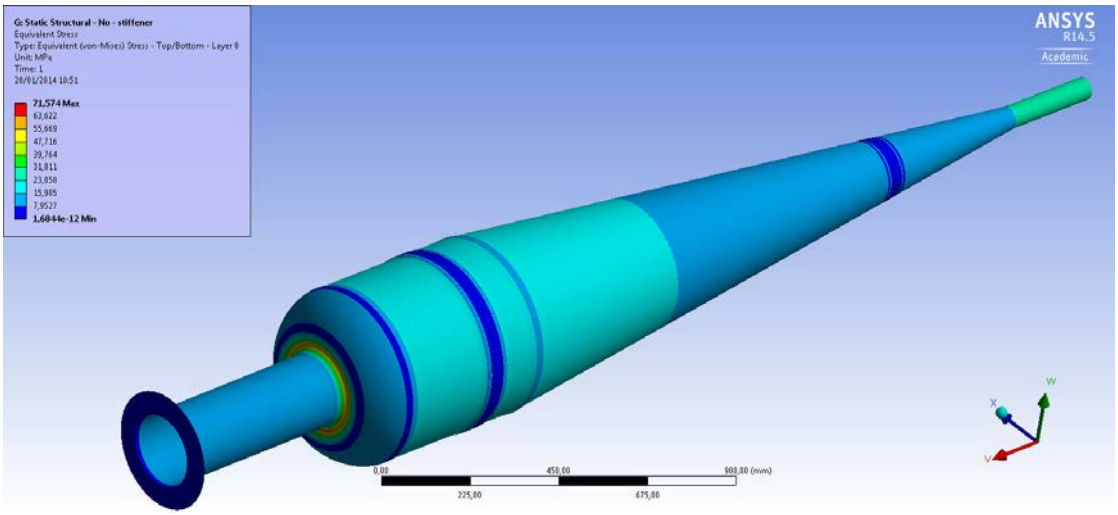


Figure 33: Von Mises equivalent stress distribution obtained with a static simulation of the beam pipe (due to symmetry only half of the beam pipe is shown). Generally, the stresses are below 50 MPa but near of the flanges they increase locally up to 72 MPa. The areas in blue exhibit the minimum stresses in the beam pipe and occur mostly where the support collars are located.

Table 7: Simulated maximum stresses on the beam pipe and comparison with the Yield stress of the material.

| Component | Maximum Stress [MPa] | Yield Stress [MPa] | Safety Factor |
|---|---|---|---|
| Beryllium cylinder | 40 | 240 | 6 |
| Stainless steel portions | 72 | 290 | 4 |

The stresses in the joint between the beryllium cylinder and the stainless steel cones are 30 MPa. In the future, this value will have to be considered in the design of this joint. The maximum displacements

occur in the flanges due to the absence of any constraint in the three axes. This result will however not correspond to the reality, since the deformations are expected to be lower due to the presence of bellows and additional supports connecting the central beam pipe to the accelerator vacuum system.

The total deformation values given by the simulation are 90 $\mu$m in the flanges and less than 10 $\mu$m in the beryllium cylinder as Figure 34 shows. In the gravity direction, as it can be observed in Figure 35, the maximum displacements are reduced to 14 $\mu$m (upwards movement) and 60 $\mu$m (downwards movement). Given the highly non-uniform deformations of the beam pipe, one can conclude that the location of the radial support spokes is not yet optimal.

The reactions in the spring supports, shown in Table 8, are not negative which yields that the pre-loads applied to them are sufficient.

Table 8: Reaction forces on the support of the beam pipe springs. The springs are divided depending on their location and orientation with respect to the z-axis, $S_n$, and position in $\phi$.

| $S_n$ | Reactions in the bottom springs [N] | Reactions in the top springs [N] |
|---|---|---|
| $S_1$ | 21.4 | 56.8 |
| $S_2$ | 76.4 | 231.7 |
| $S_3$ | 40.3 | 98.9 |

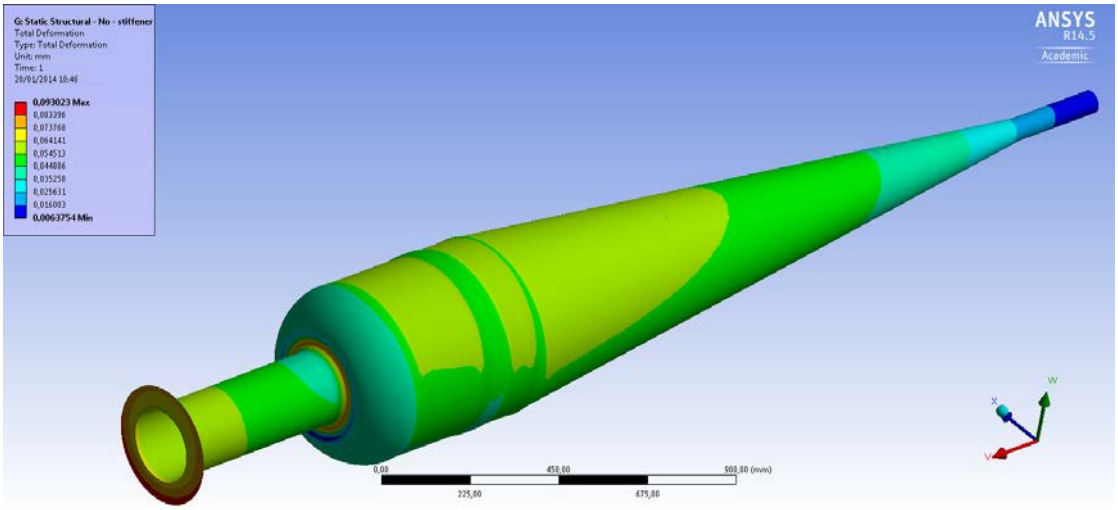


Figure 34: Total deformations of the beam pipe. The maximum displacements are located in the flange region, with values of 90 $\mu$m, and the minimum ones are located mostly in the beryllium cylinder, with values lower than 10 $\mu$m.

The results obtained from the mechanical linear buckling analysis are shown in Figures 36 and 37. The buckling simulation of the proposed beam pipe geometry yields a load multiplier of 0.81, which would mean that buckling will already occur below atmospheric pressure ($0.81 \cdot 10^5$ Pa). Furthermore, given that a linear buckling analysis does not take into account any geometrical imperfections or non-linearities in the structure, the results are not conservative. A future detailed analysis, which is expected to result in a load multiplier even lower than 0.81, will require a non-linear buckling simulation.

The analysis of the buckling mode shape shows that the beam pipe will fail in its conical portion. In order to improve the stiffness of this region, the wall thickness of the beam pipe may be increased

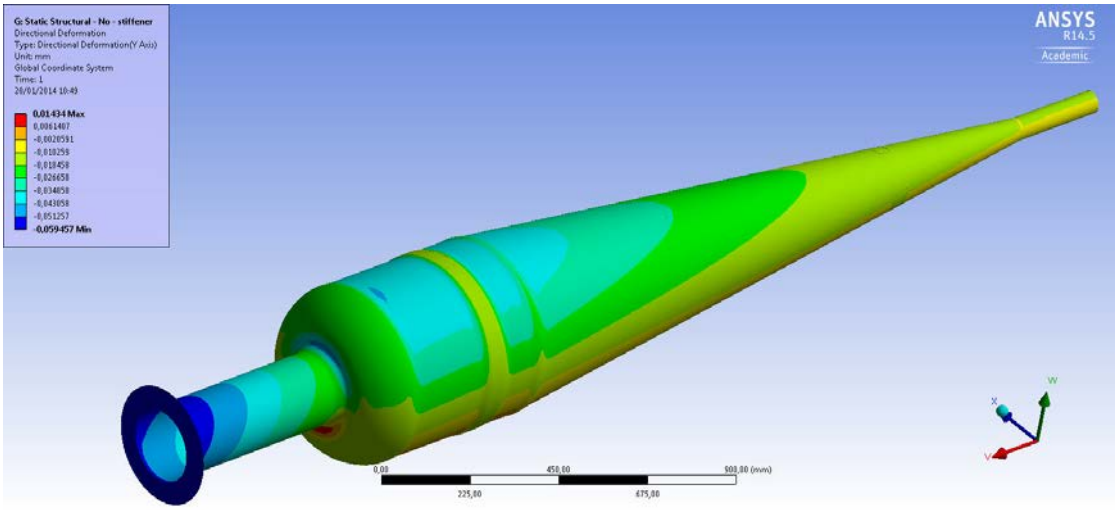


Figure 35: Beam pipe deformations along the gravity direction. The bottom of the beam pipe in the central region experiences upward displacements with a peak value of 14 $\mu$m while in the forward region the displacements are mostly in the downwards direction, with a peak value of 60 $\mu$m. This indicates that the location of the radial support spokes is not optimal.

and/or local stiffeners may be added as proposed for the beam pipe of the ILC ILD detector concept [12]. At this stage, two options have been simulated: (1) having a conical (steel) section of the beam pipe with a wall thickness of 1 mm and a 1 mm thick reinforcement ring, or (2) having a beam pipe with a wall thickness of 1.5 mm and two 2 mm thick reinforcement rings on the conical portion. In both cases the reinforcement rings were added in the location where the buckling occurs. The results of the linear buckling simulation, illustrated in Figure 37, show that for the first option the load multiplier is increased to 1.07 while for the second option the value increases to 5.8.

Another possible solution would be to increase even further the thickness of the conical portions of the beam pipe, at the expense of an increase in the beam pipe's mass. Furthermore, one can also think about optimising the location of the beam pipe support collars such as to increase its buckling strength. Further studies will be needed in order to assess the feasibility of the proposed solutions, as well as their impact on the performance of the cooling system.

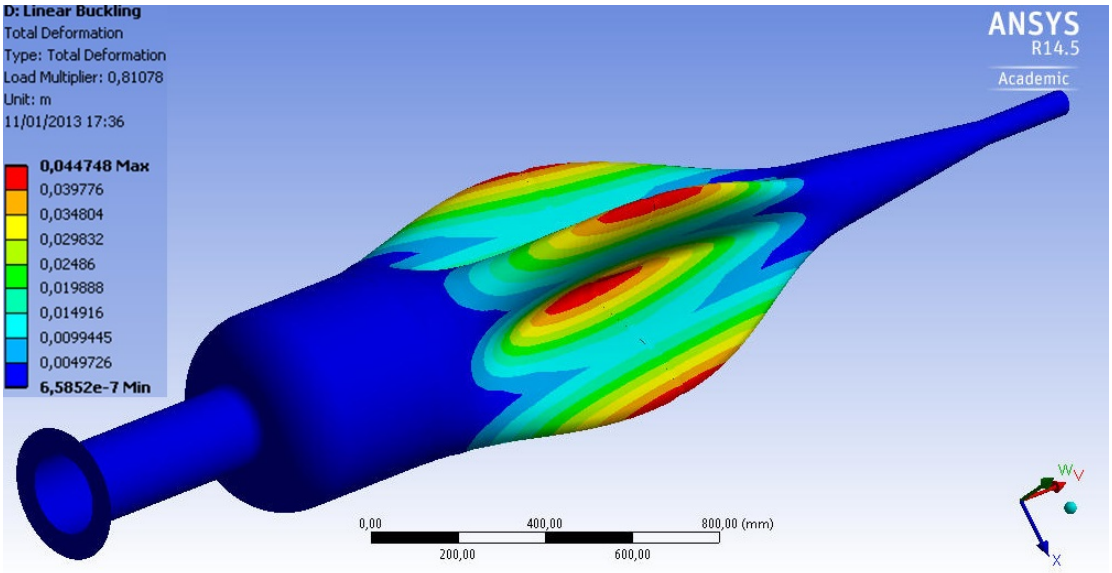


Figure 36: Results from the linear buckling simulation of the beam pipe. The load multiplier is 0.81 which means that the beam pipe would buckle at a pressure of $0.81 \cdot 10^5$ Pa.

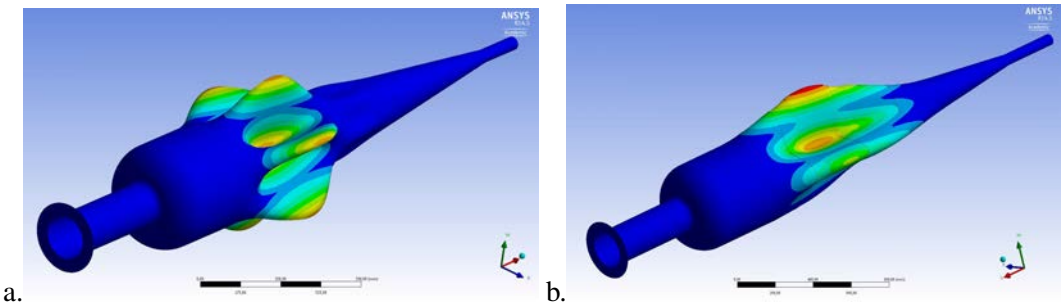


Figure 37: Results from the simulations of two possible solutions to increase the buckling strength of the beam pipe. a) Beam pipe with a wall thickness of 1 mm and a 1 mm thick reinforcement ring on the conical portion (load multiplier of 1.07) and b) beam pipe with a wall thickness of 1.5 mm and two 2 mm thick reinforcement rings on the conical portion (load multiplier of 5.8).

# 7 Appendix C: Cabling Layout

## 7.1 Introduction

This appendix describes a possible cabling layout of the vertex detector elements and the innermost tracking detectors in a CLIC detector, studied here for the example of the CLIC_ILD concept [1]. The note also provides information on the total amount of material due to the cables, and emphasises address some of the challenges:

- How to pass cables through support structures and past sub-detector elements without modifying the dimension and position of the sensors;
- How to find a compromise between minimal material budget and cabling through the support structures;
- How to optimise cable bending and to make sure damage to the cables is avoided[3] .

In § 7.2, a description of a type of flat cable possibly to be used in the central region of a CLIC detector is presented. In § 7.3, the cabling layout is described per subdetector, from the outer to the inner parts of the tracking and vertex region. This corresponds to the order in which the sensors would be installed and cabled, and at the same time this sequence implies that the least challenging layouts will be described first. The order of the subsections is Silicon Internal Tracker SIT2, followed by SIT1, Vertex Endcap (VXEC) and Vertex Barrel Detector (VXBD). The Forward Tracker Disks (FTD) cabling layout is described in the last subsection of § 7.2.

## 7.2 Description of a Proposed Cable

The cables presently proposed to power the Front End (FE) electronics of the detectors are low mass flexible cables. Their conductive material is aluminium which reduces the material contribution by a factor of 4 compared to copper cables with the same total electrical resistance. These cables are composed of 6 layers of different material with a total thickness of 140 $\mu$m as shown in Figure 38a. Three different materials are used: two aluminium layers to conduct electricity to power the sensors, three kapton layers to provide the desired mechanical properties and electric isolation and 1 glue layer to glue the intermediate layers. Figure 38 shows the different layers and their thickness in $\mu$m as well as a photograph of such a cable.

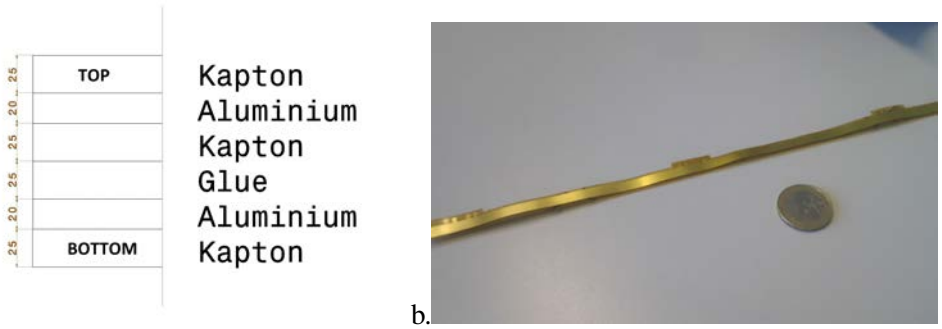


a. b.

Figure 38: a) Schematic cross section of the cable showing the different material layers and their thickness in $\mu$m. The kapton layers are used to electrically isolate the aluminium layers and to provide the desired mechanical strength. b) Image of a real 10 mm wide Flex cable.

[3] Cable bending simulations are discussed in [13].

The cable distribution presented in this section follows the powering scheme shown in Figure 39. The vertex detectors and inner trackers will be powered from both sides of the inner region in order to decrease the current through the cables. The flexible cables described in this section correspond to the "30 cm AL cable" indicated in Figure 39 [4].

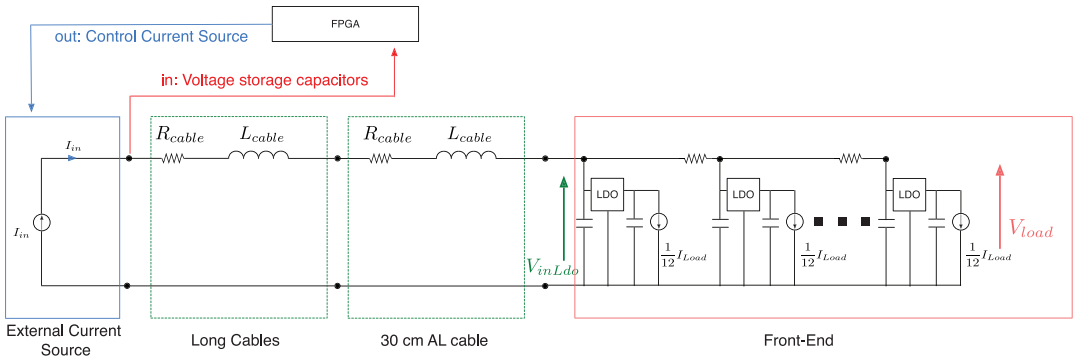


Figure 39: Powering scheme proposed for a half ladder of the vertex detector (from [14]).

[4] The length of 30 cm is a remnant from an earlier design - these flexible cables could be longer, but at some point, where the material budget starts to be less critical, one would want to change to another type of cable.

## 7.3 Cabling Layout for the different Sub-Detectors

### 7.3.1 Silicon Inner Tracker - SIT2

The SIT 2 cables are the first ones to be installed in the Main Support Cylinder. Figure 40 shows the cabling layout for half of the cylinder. The cables start at the SIT2 detectors, and run along the inner wall until they arrive at the end of the cylinder. The total length of a cable from a SIT2 detector to the edge of the Inner Support Structure is about 1.65 m. More technical details on the SIT2 detectors are needed in order to define a dedicated CFRP structure to support them, and to decide on the final SIT2 cabling layout and routing.

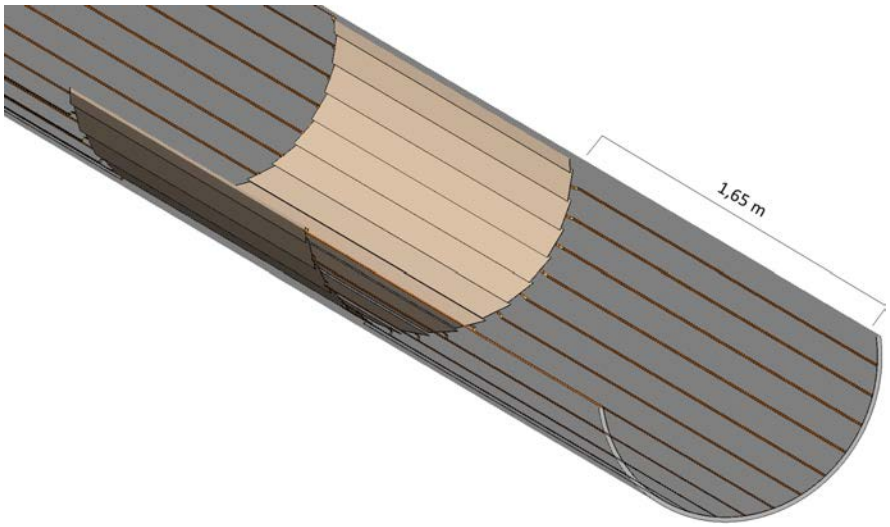


Figure 40: 3D view of the cabling layout of the SIT2 inside the Main Support Cylinder. In the center of the image the SIT2 sensors are shown.

### 7.3.2 Silicon Inner Tracker - SIT1

The next cables to be installed according to the assembly sequence (see section 3) are those related to the SIT1 detectors, as shown in Figure 41. The total length of such a cable is about 2 m. The cables start at the SIT1 detectors and follow the Outer Support Structure which supports the VXD and the SIT1. After they reach the Main Support Cylinder, they run alongside it and out to the edge of the cylinder. At this stage, the cables lay on top of the SIT2 cables installed previously. In order to avoid any interference between the cables and the carbon fiber supports and to avoid obstructing the openings in the carbon fiber cylinder (to allow the natural convection to air-cool the FTD [15]), the layout proposed here must be re-visited in future versions of the CLIC detector design.

### 7.3.3 Vertex Detector Endcaps - VXEC

The VXEC cabling layout is more complex because the nearer the sensors are to the IP, the more support and sensor layers their cables have to pass to reach the outer edge of the Main Support Cylinder. The external radius of the VXEC petals is 102 mm and the radius of its support is 105 mm. This difference of 3 mm allows the cables to cross the openings in the CFRP petals without modifying the VXEC geometry, as shown in Figure 42. The cables are glued to the interior wall of the Inner Support Structure, which supports the VXEC and VXBD. They run outwards until they arrive at the Outer Support Structure and follow its shape. Finally, they follow the inner side of the Main Support Cylinder. Figure 43 shows the

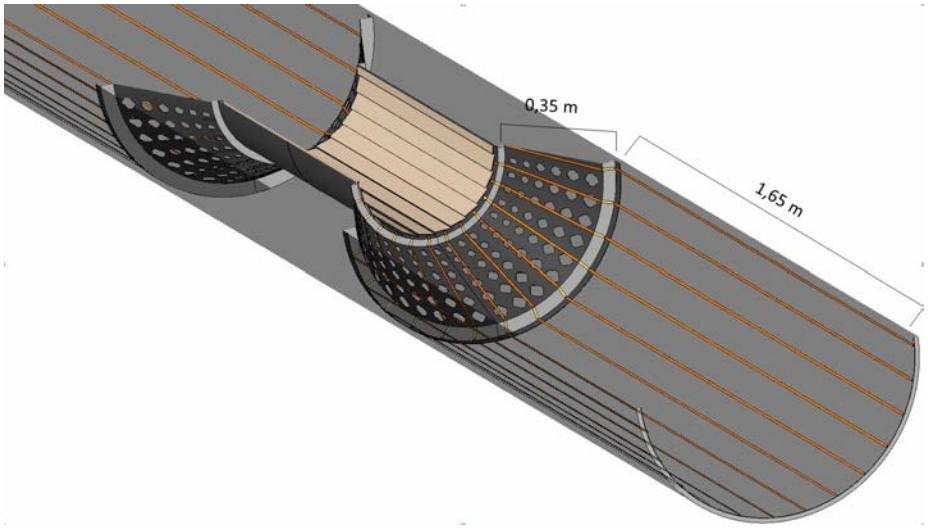


Figure 41: 3D view of the cabling layout of the SIT1. In the centre of the image the Outer Support Structure and the SIT1 detectors are shown. The remaining elements are hidden for clarity of the picture. The Flex cables follow the shape of the perforated structure and finally arrive to the edge of the Main Support Cylinder.

detailed layout for the routing of the VXEC cables. The average total length of a cable going from a VXEC to the edge of the Main Support Cylinder is about 2.1 m. The routing of the cable is complicated, since one tries to avoid any superposition with other detector elements.

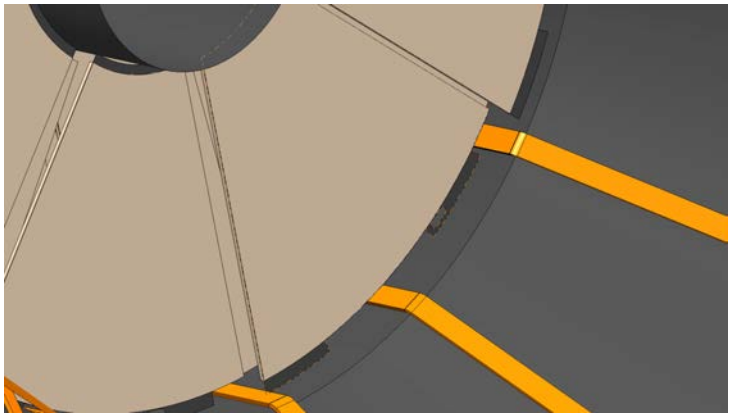

Figure 42: Detailed 3D view of the openings in the VXEC Petal Support, designed to allow the cables to cross it. Some apertures are wider than others because additional space is needed for the VXBD cables.

### 7.3.4 Vertex Detector Barrel - VXBD

**Change of the number of ladders in the VTX barrel** In [3] and [1] the number of ladders for the Vertex Barrel of CLIC_ILD is given as 18 for the inner double layer, 13 for the middle one and 17 for the outer one. Since there is no cable layout pattern that easily matches these numbers, the number of the ladders has been modified for the present study, in order to allow the cables to match and stack up with one another.

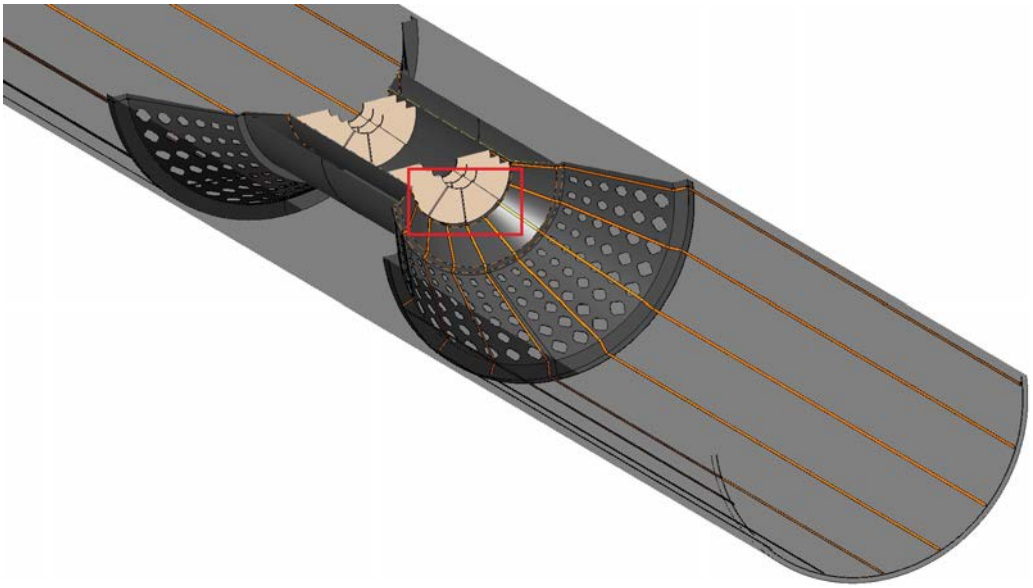

Figure 43: 3D view of the VXEC cabling layout. The cables have to follow a complex path with substantial local bending in order to follow the shape of the different CFRP support structures. For clarity, only one half of the Inner Support Structure and of the VXEC detectors is shown. The other components are hidden. The red rectangle indicates a region which is shown in more detail in Figure 42.

We point out that it is problematic to stack up the cables with the layout of the CDR for two main reasons. First, there would be the need to bend the cables in a very small space of 30 mm (see Figure 44), in two different planes from the detector to the CFRP supports. In such a scenario, a heavy twist on the cables would be required. Second, the CDR proposal would lead to a multitude of different cable and CFRP structure geometries, which would considerably complicate the design and construction of the detector.

The solution proposed consists of spreading out the cables in a way intermediate to the two cases shown in Figure 45. For the case of maximum spreading out (see Figure 45a), the area to assemble the supports for the VXEC is minimal, cables have minimal twist and the CFRP structures all have different geometries. On the other hand, for the case of minimum spreading out (Figure 45b) the stacking up of cables is maximal (a stack of cables would be about 4 mm thick, including the VXEC cables) so the material budget increases locally in specific angular regions, and the cables need to be strongly twisted.

A new VXD layout with 16-12-16 ladders is proposed, where the number of different paths around the whole cylinder is 24, instead of 48 as in Figure 45a or 8 different paths as in Figure 45b. This new layout allows to reduce the local amount of material due to cables to less than 2 mm, while using a layout that follows the VXEC cabling, see Figure 46.

With this strategy, the cables do not spread out as shown in Figure 45a, they cross the detector using the same openings as the VXEC cables - an engineering compromise between the spacing of mechanical supports, the twist of the cables and the apertures for cables. As drawback, there is a cable stack of 2 mm thickness in some openings, which could reduce the momentum and impact-parameter resolutions [16]. It is important to define the limit of the maximum amount of cables in a given region in terms of physics performance.

The change in the total number of sensors (ladders) does not affect their radial distance from the IP nor the overall geometry of the detector[3], the only geometric change being the angle between sensors

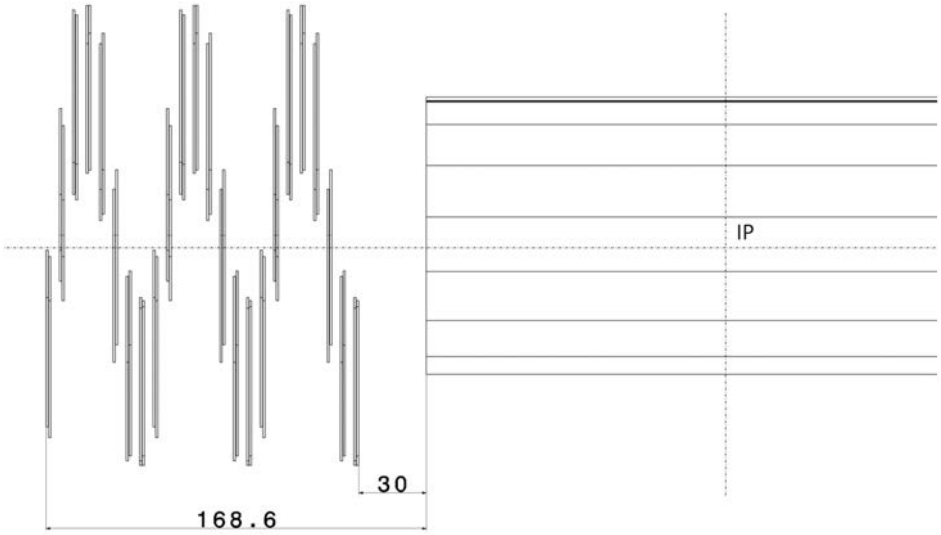


Figure 44: 2D drawing of the distance (given in mm) between the first and the last VXEC detector and the VXBD. The small distances imply a big challenge to extract the cables. The dashed lines represent the axes of the detector which intersect at the IP.

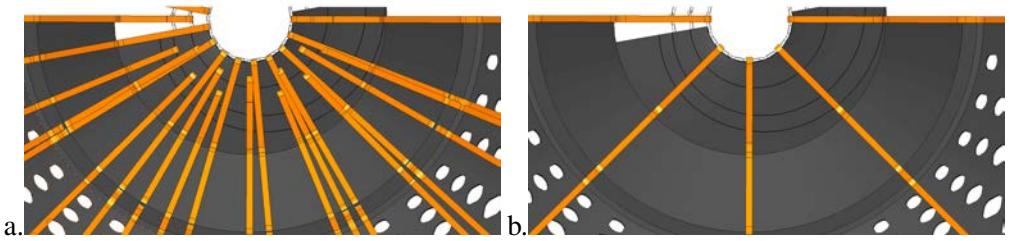


Figure 45: Front view of the extreme VXBD layout cases of a) maximum spreading out of cables with the number of ladders 18-13-17 and b) minimum spreading out with the same number of ladders, 18-13-17. It implies heavy twists in the cables in order to follow the same path and a 4 mm cable stack up. (The picture shows only the bottom half of the front face.)

and the particle trajectory. Further studies are required to verify whether this change is important or not, i.e. if and how it affects the data.

**VXBD Cabling Layout** The VXBD cables are the closest ones to the IP. As a result, they have to cross several other layers of the inner tracking region. Openings in several carbon fiber structures are needed for these cables. Furthermore, the cables must be fixed as close as possible to the CFRP walls in order not to perturb the air flow[15].

As is shown in more detail in Figure 48, the VXBD cables fit in the same apertures provided initially for the VXEC cables and shown in Figure 42.

In Figure 49 the layout of the combined VXBD and VXEC cabling is shown. For comparison, in Figure 50 the SIT1 and SIT2 have been added and the complexity of the cabling can be appreciated. There are a lot of cables, and they all could interfere with sensors or with the apertures needed to cool the FTD, the SIT1 and SIT2. A more detailed study will be needed in order to verify the integration, the layout and the cooling process of all sub-detectors. This study must be performed in parallel with further

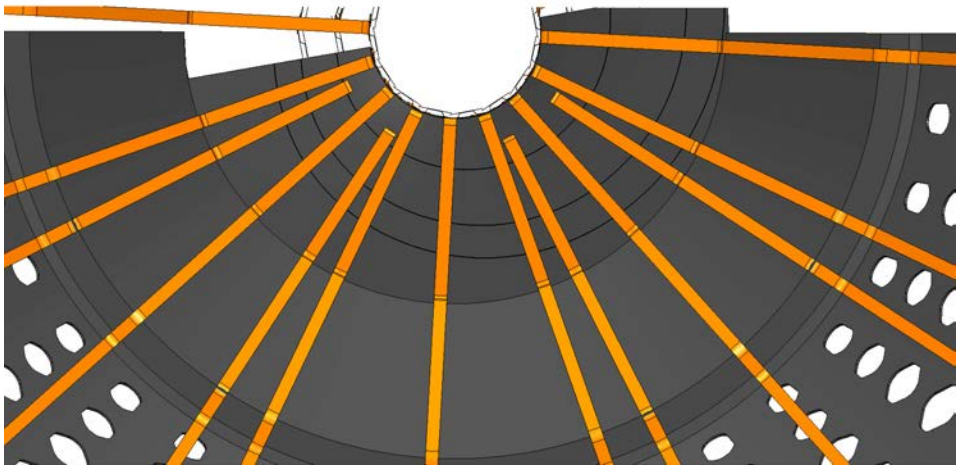

Figure 46: Proposed cable layout for the number of VXBD ladders of 16-12-16. (Only the lower half of the front face is shown.)

a. 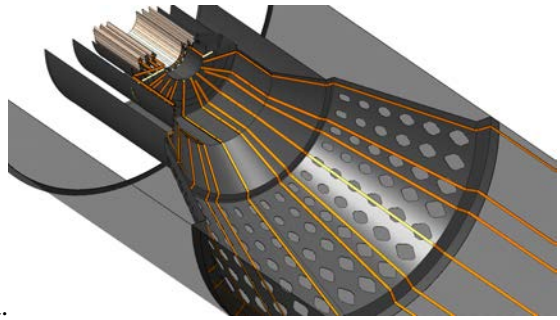 b. 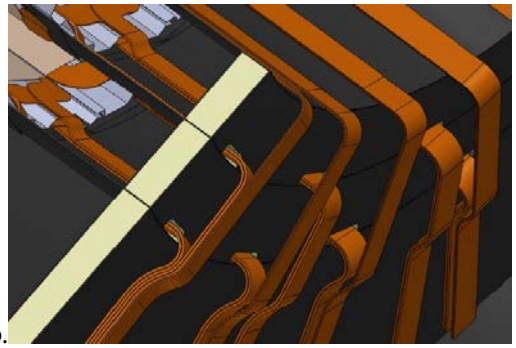

Figure 47: a) Chosen VXBD cabling layout that matches the VXEC cabling layout and b) detail of thecable passages in the VXBD Barrel Supports.

work on sensors and support structures.

#### 7.3.5 Forward Tracking Disks - FTD

The FTD sensors are the only ones to be assembled differently, i.e. around the stainless steel Conical Shields of the beam pipe. Details of CFRP supporting frames (half-rings) for the sensors remain to be studied. The FTD1 cables are first installed, see Figure 51a. The number of cables of that detector is likely to be larger than for the other FTDs because of the different detector technology envisaged, as explained in § 7.2.

The next detectors and their cables are assembled sequentially from inside to outside (Figure 51b), first the FTD2, followed by the FTD3, etc., stacking up all FTD cables on top of eachother.

In Figure 52 a detail of the FTD cable stack is shown, with the FTD1 cable at the bottom and the FTD5 cable at the top. Each time the cable path crosses an FTD, the thickness of the cable stack increases.

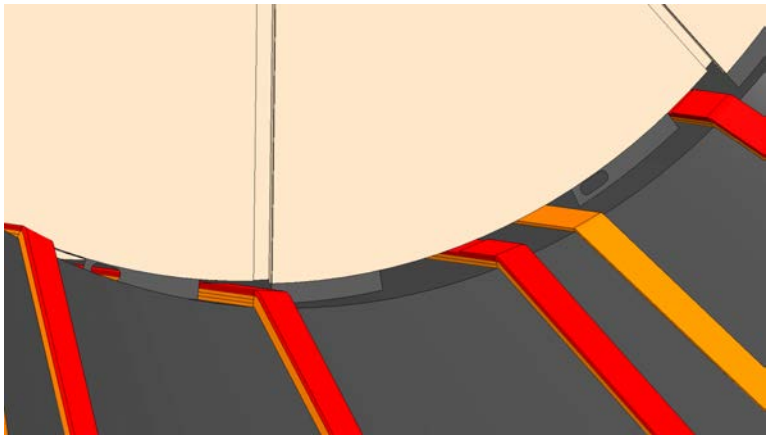

Figure 48: Detail of the overlap of VXEC cables (in red) with the VXBD cables (in orange). There are two different sizes of openings in the Petal Supports, to produce only one type of supports and make their design compatible with the cabling layout.

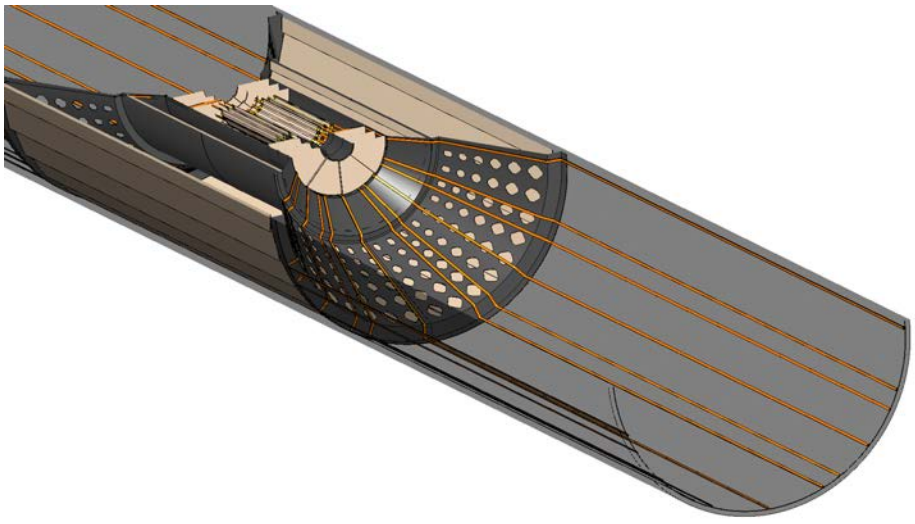

Figure 49: View of the combined VXEC and VXBD cabling layout in one half of the Inner Support Structure.

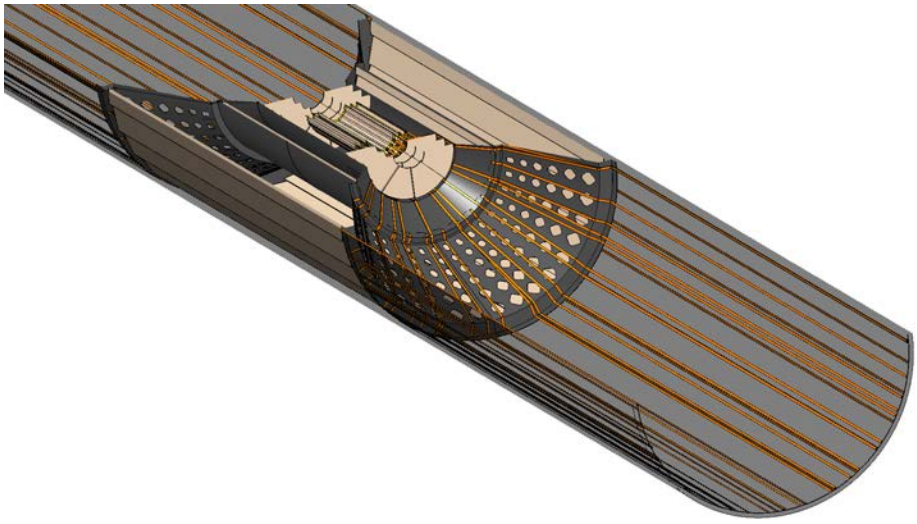

Figure 50: Global vision of all the cables mentioned before in one half of the Inner Support Structure of the inner region. It includes the VXBD, the VXEC, the SIT1 and SIT2 cables.

a. b.

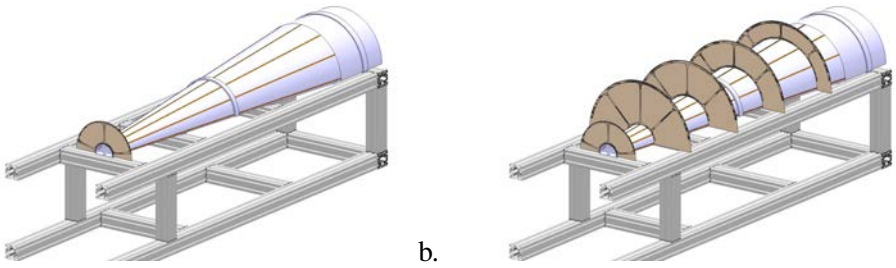

Figure 51: 3D view of the FTD cabling layout. Only one half of the Conical Shields is shown, on a temporary support designed for the assembly of the FTDs with the Conical Shields. a) Cabling layout for the FTD1 and b) cabling layout for the complete FTD system with, from left to right, FTD1, FTD2, FTD3, FTD4 and FTD5.

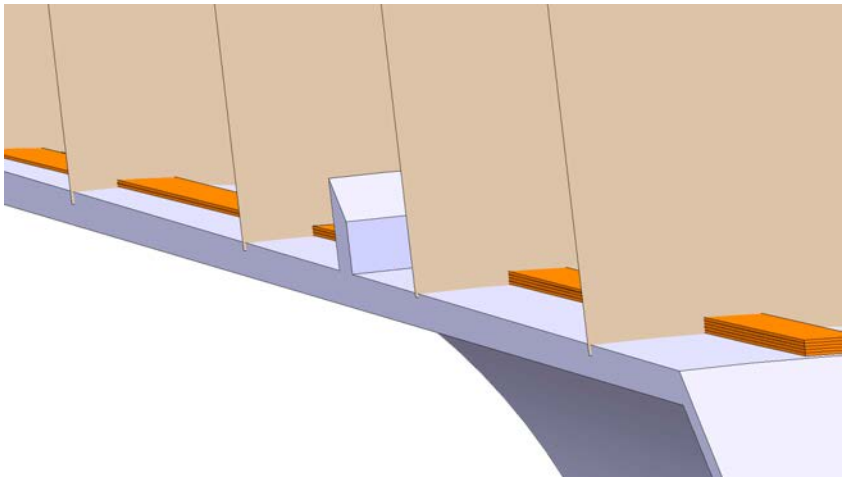

Figure 52: Detail of the FTD cable stack. The stainless steel Conical Shield is shown in blue. The orange elements are the cables. The total thickness of the cable stack increases every time an additional FTD (in brown) is crossed. The apparent interference of the FTD with the stainless steel outer Conical Shield is an artefact due to the graphical resolution used in the CAD program.

# 8 Appendix D: Material Budget Calculations

The physics requirements for CLIC demand an excellent track-momentum resolution and an efficient tagging of decays involving heavy quarks by reconstructing their displaced vertices. To achieve these requirements, the material budget as well as the number and the placement of the detector layers and their single-point resolutions, are the main factors determining the vertex detector performance [16]. It is then of particular importance to use a realistic material budget, based on the engineering layout, in the detector performance simulation studies.

This section provides an estimate of the total amount of material in the detector, measured as a fraction of the radiation length $X_0$, versus the polar angle $\theta$ or azimuthal angle $\Phi$ as defined in Figure 53.

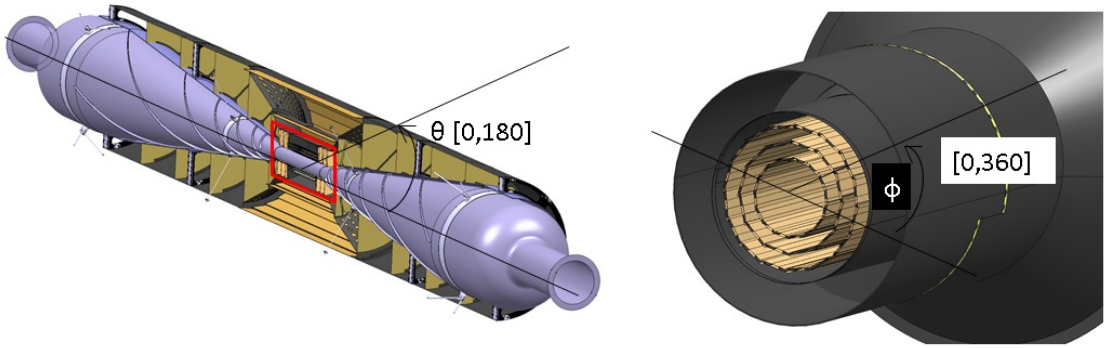


Figure 53: View of the polar angle $\theta$ and azimuthal angle $\Phi$ along which the material budget was calculated. On the left, the angle $\theta$ varies between 0° and 180° in the detector y-z plane. The volume inside which the material budget was calculated is shown in red. On the right, the angle $\Phi$ varies between 0° and 360° in the detector x-y plane (at z=0).

## 8.1 Material budget in the physics simulations

For the elaboration of the CLIC CDR, simulations had been performed in order to estimate the radiation length of the inner region, including the amount of material in the VXD, the beryllium beam pipe, the cables and the CFRP structures. The amount of material at polar angle $\theta = 90°$ was estimated to $0.85\%X_0$ [3]. The values used for the material budget of each elelment in the physics simulations are shown in Table 9. A third column in Table 9 shows the values mentioned in the CDR as a realistic target for all the elements inside the vertex detector region, based on the proposed hybrid pixel detector technology. As can be seen, values deemed realistic in the CDR are almost twice the ones used in the physics simulations.

The layout of the elements used in the simulations for the CDR is shown in Figure 54a. The double layers include the VXBD, shown in dark green, and the CFRP supports between them, shown in black. The support structure is made of CFRP and the beam pipe is made of beryllium. The corresponding estimated value of the material budget as a function of the polar angle $\theta$ is shown in Figure 54b.

## 8.2 Material budget in the engineering model

Section 2 of this paper describes the detectors and the support structures within the vertex detector region. The amount of cables as well as their assumed materials, dimensions and positions are presented in

Table 9: Material budget values used in the physics simulations at the polar angle $\theta$ =90°.

| Component | X/$X_0$ CDR physics simulations | X/$X_0$ CDR realistic values |
|---|---|---|
| Beryllium beam pipe | 0.17% | 0.17% |
| Double layers 1-2 | 0.18% | 0.40% |
| Double layers 3-4 | 0.18% | 0.40% |
| Double layers 5-6 | 0.18% | 0.40% |
| Support Structure | 0.14% | 0.14% |
| TOTAL | 0.85% | 1.51% |

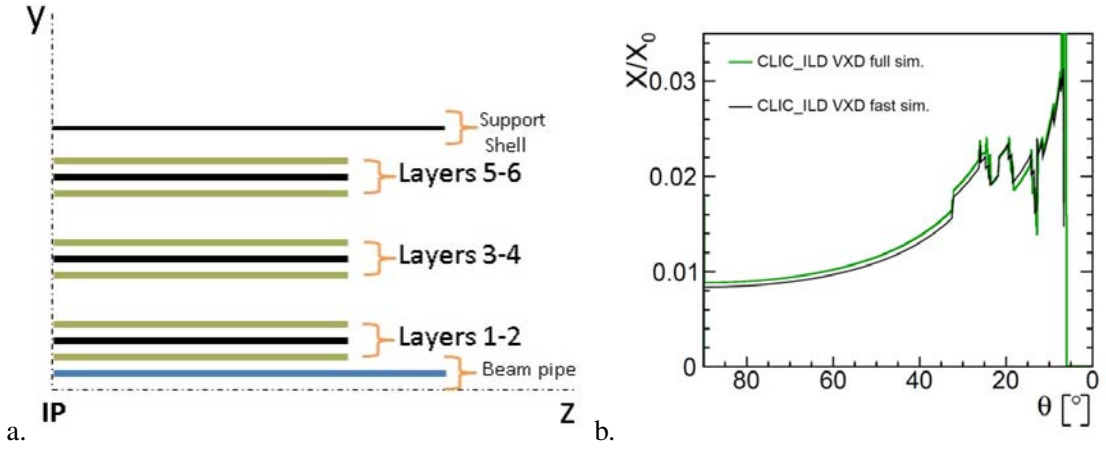


Figure 54: a) Layout of the elements used in the estimation of the material budget for the physics simulations; b) material budget versus the polar angle $\theta$ for the CLIC ILD simulation model. Due to the conical beam pipe, the material budget peaks at $\theta \approx 7°$ (from [3]).

Appendix C. A summary showing the thickness of the main components considered for the calculation is given below.

### 8.2.1 Thickness of the main components

Table 10 shows the thickness of each component in a vertex detector barrel stave according to the layout established in Figure 55. Given that the material budget of the components for power delivery and power pulsing (LDOs, capacitors and flex cables) has already been estimated [14], the thickness for these components has been replaced in the calculations by the material budget estimated (0.043% $X_0$).

Given that the design of the petals is not as advanced as the one of the barrel staves, a detailed layout for the petals is not yet available. However, since both will share the same pixel technology, for the purpose of this study it was considered that the layout of the petals will be identical to the one of the barrel staves with the difference being in the type of support structure used. Table 11 shows the thickness of each component in a vertex detector endcap petal according to the layout established in Figure 56. Similarly, the thickness of the LDOs, capacitors and flex cables has been replaced in the calculations by the material budget estimated in [14], i.e. 0.043% $X_0$.

Table 10: Thickness of each component in a double-sided VXBD stave used for the calculation of the total material budget.

| Component | Thickness [$\mu$m] |
|---|---|
| Readout ASIC (Si) + Sensor (Si) | 50 + 50 |
| Glue (epoxy) | 25 |
| LDOs + capacitors + Flex cable | - |
| Glue (epoxy) | 25 |
| Support Structure (CFRP) | 100 |
| Glue (epoxy) | 25 |
| LDOs + capacitors + Flex cable | - |
| Glue (epoxy) | 25 |
| Readout ASIC (Si) + Sensor (Si) | 50 + 50 |

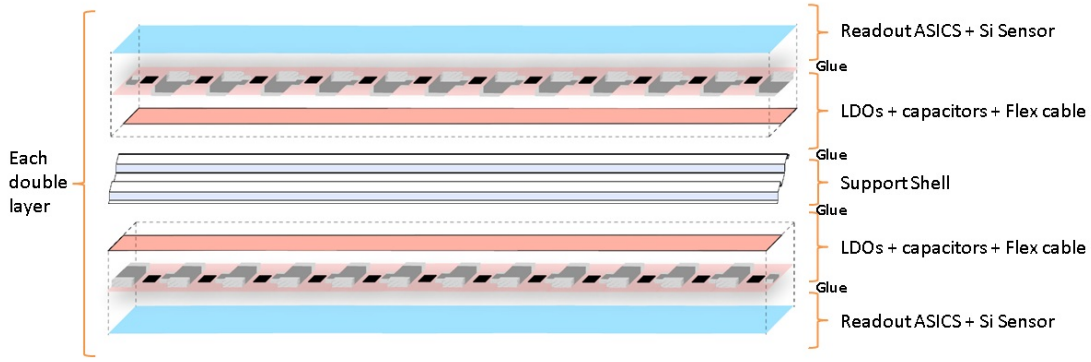


Figure 55: Layout of each VXBD double-sided stave.

A 3D partial view of the cable layout in the vertex detector is shown in Figure 57a. As it can be seen, the contribution of the cables to the material budget follows a discrete pattern in $\Phi$. The composition of a cable and the thickness of each of its components is listed in Table 12. In order to simplify the calculation and the comparison with the material budget used in the physics simulations, the thickness of the cables has been homogenized along the $\Phi$ angle, as shown in Figure 57b.

Table 11: Thickness of each component in a double-sided VXEC petal used for the calculation of the total material budget.

| Component | Thickness [$\mu$m] |
|---|---|
| Readout ASIC (Si) + Sensor (Si) | 50 + 50 |
| Glue (epoxy) | 25 |
| LDOs + capacitors + Flex cable | - |
| Glue (epoxy) | 25 |
| Support Structure (CFRP+Rohacell+CFRP) | 120 + 1500 + 120 |
| Glue (epoxy) | 25 |
| LDOs + capacitors + Flex cable | - |
| Glue (epoxy) | 25 |
| Readout ASIC (Si) + Sensor (Si) | 50 + 50 |

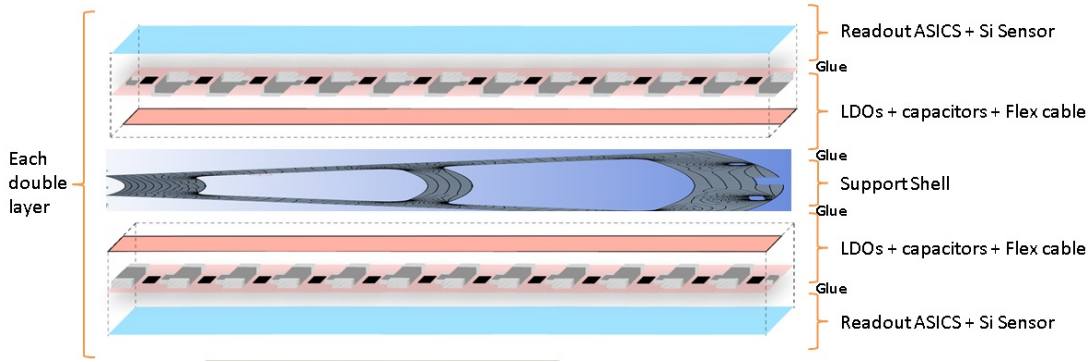


Figure 56: Layout of each VXEC double-sided petal

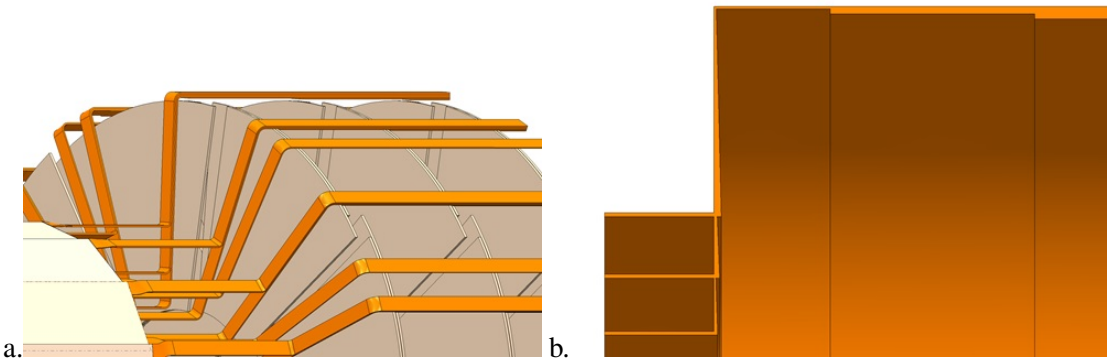


Figure 57: Cable layout in the vertex detector. a) The real cable layout showing a contribution to the material budget that follows a discrete distribution in $\Phi$. b) Geometrical simplification of the cable layout (for the purpose of the material budget calculations) done by homogenizing the thickness of the cables in $\Phi$.

### 8.2.2 Methodology

With the preliminary design of the main components in the vertex detector volume, it is possible to calculate the material budget of the engineering model and compare it with the CDR target values listed in Table 9. For the calculation, a plug-in software created by IN2P3 was used. It works directly with the 3D CAD software CATIA v5 (employed to model the vertex detector region). This plug-in was used in the past, e.g. for the material budget calculations of the ATLAS IBL upgrade, showing good results [17]. The software does not use GEANT4.

The plug-in, a sequence of instructions addressed to CATIA to create points and the corresponding connecting lines, gives as an output the thickness of each element of the geometry. It requires the

Table 12: Layout of a vertex detector cable with the thickness of each component.

| Component | Thickness [$\mu$m] |
|---|---|
| Kapton (polyimide) | 25 |
| Aluminium | 20 |
| Kapton (polyimide) | 25 |
| Glue (epoxy) | 25 |
| Aluminium | 20 |
| Kapton (polyimide) | 25 |

definition of the origin point in the CAD coordinate system, in our case the IP, and the different intervals of $\theta$ (from $\theta$=0° to $\theta$=180° ) and $\Phi$ (from $\Phi$=0° to $\Phi$=360°). Once the thickness of each element is calculated, it is possible to obtain the fraction of the radiation length for each angle using the expression:

$$\frac{X}{X_0} = \Sigma_i \frac{\rho_i \cdot d_i}{X_{0_i}} \tag{2}$$

where, for each material i, $X_{0_i}$ is the the radiation length in $g/cm^2$, $\rho_i$ is the density and $d_i$ is the thickness obtained with the CATIA plug-in. Steps of $\Delta\theta$=0.02° and a $\Delta\Phi$=0.02° have been considered sufficiently small for the present study. The radiation length of the materials used in the physics and engineering models are shown in Table 13.

Table 13: Radiation length of the different materials used in the physics and engineering models

| Material | Radiation length $X_0$ $[cm]$ |
|---|---|
| Beryllium | 35.3 |
| Silicon | 9.4 |
| CFRP | 25.7 |
| Rohacell | 544.0 |
| Aluminium | 8.9 |
| Polyamide | 28.6 |
| Epoxy | 35 |

### 8.2.3 Results

Two material budget calculations of the vertex detector have been done in order to estimate the amount of material in the current engineering model. In the first one, the angle $\Phi$ has been fixed at 90° and the material budget versus $\theta$ was calculated. For the second calculation, the angle $\theta$ was fixed at 90° and the material budget versus $\Phi$ was calculated.

#### Material budget vs. $\theta$

The individual contribution to the material budget of the silicon, epoxy and power pulsing components in the vertex detector is plotted in Figure 58 as a function of the angle $\theta$. The different peaks that appear in the forward region are labelled in Figure 59 and the layers that contribute to them identified in Table 14.

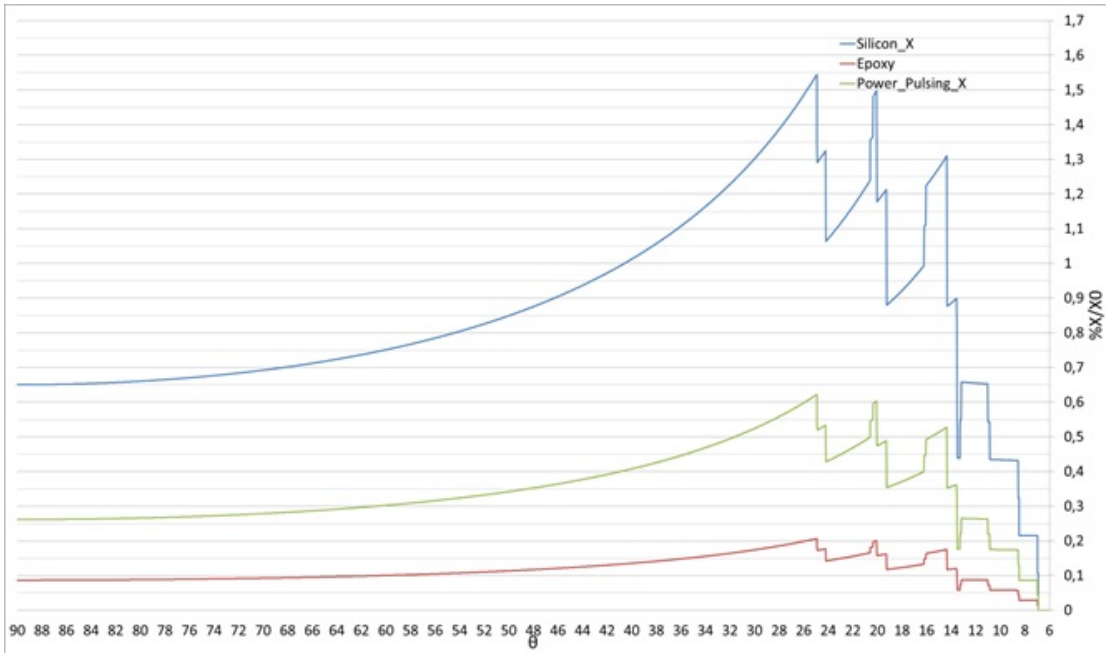


Figure 58: Contribution to the material budget of the silicon, epoxy and power pulsing components in the vertex detector, according to the engineering model. The most important contribution is from the six 100 $\mu$m thick layers of silicon (sensor and ASIC).

From the analysis of Table 14, in the current design, for $\Phi = 90°$, there are between 5 and 6 sensitive layers for every angle $\theta$ between 7° and 90°, with some exceptions:

- In the angles between $\theta = 24°$ and $\theta = 20°$ there is only a coverage of 4 sensitive layers (VXBD 1-4);
- In the angles between $\theta = 19°$ and $\theta = 16°$ there is only a coverage of 4 sensitive layers (VXBD 1-2 and VXEC 1-2);
- In the angle $\theta \approx 13°$ there is only a coverage of 4 sensitive layers (VXEC 1-4);
- In the lowest angles, from $\theta = 11°$ to $\theta = 7°$, there is only a coverage of 4 or less sensitive layers.

Figure 60 shows the contribution of the cables to the material budget as a function of the angle $\theta$ considering, for simplification purposes, the homogenized cable layout shown in Figure 57b. In reality,

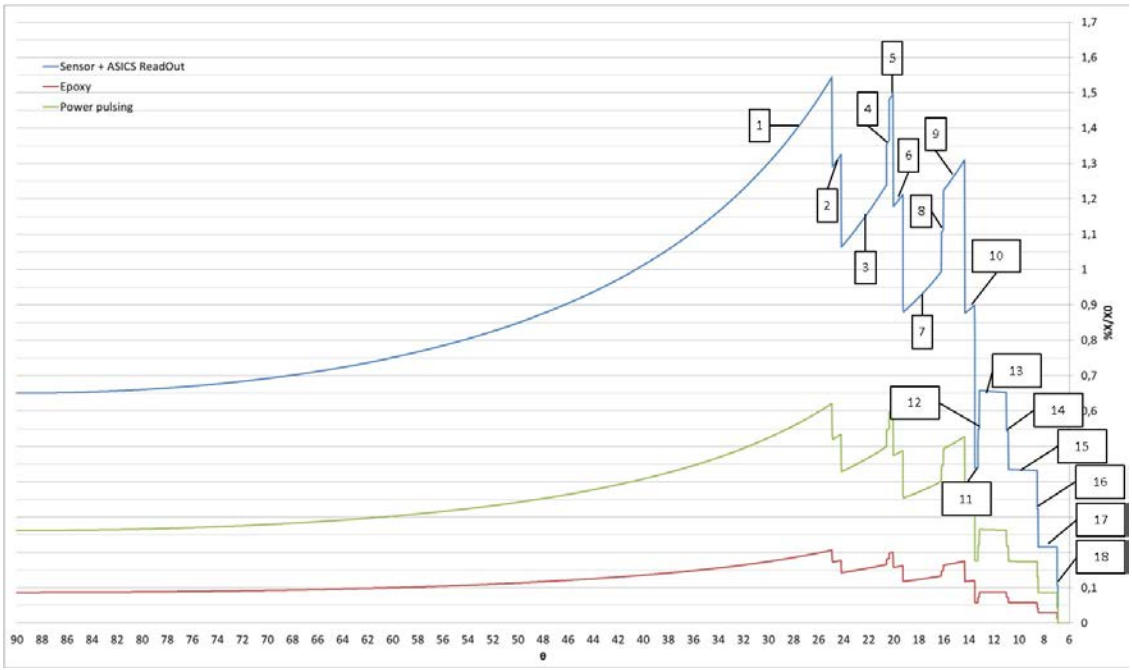


Figure 59: Contribution to the material budget of the silicon, epoxy and power pulsing components in the vertex detector, according to the engineering model. The labels identify the different peaks.

Table 14: Identification of the peaks seen when plotting the contribution to the material budget of the silicon, epoxy and power pulsing components in the vertex detector, according to the engineering model.

| Label number | Layers | Label number | Layers |
|---|---|---|---|
| 1 | VXBD 1-6 | 10 | VXBD 1 + VXEC 1-4 |
| 2 | VXBD 1-5 | 11 | VXEC 1-4 |
| 3 | VXBD 1-4 | 12 | VXEC 1-5 |
| 4 | VXBD 1-4 + VXEC 1 | 13 | VXEC 1-6 |
| 5 | VXBD 1-4 + VXEC 1-2 | 14 | VXEC 2-6 |
| 6 | VXBD 1-3 + VXEC 1-2 | 15 | VXEC 3-6 |
| 7 | VXBD 1-2 + VXEC 1-2 | 16 | VXEC 4-6 |
| 8 | VXBD 1-2 + VXEC 1-3 | 17 | VXEC 5-6 |
| 9 | VXBD 1-2 + VXEC 1-4 | 18 | VXEC 6 |

due to the layout of the cables, there is an accumulation of material in certain $\Phi$ angles and a reduction in others. In the future, this must be taken into account in order to assess the effect of the cables on the physics performance of the detector. The flex cables inside the VXBD staves and VXEC petals are not included in this calculation as they are replaced by a uniform value of 0.043 $X_0$ as estimated in [14].

The calculated material budget for the support structures of the vertex detector, including the Inner Support Structure described in 2.2.3, is shown in Figure 61. Between the angle $\theta = 20^\circ$ and $\theta = 24^\circ$ there is a peak corresponding to the conical portion of the Inner Support Structure. Since this structure is located outside of the vertex detector region, this peak will not affect the physics performance of the vertex detector. The total material budget in the vertex detector as a function of the angle $\theta$ is shown in Figure 62.

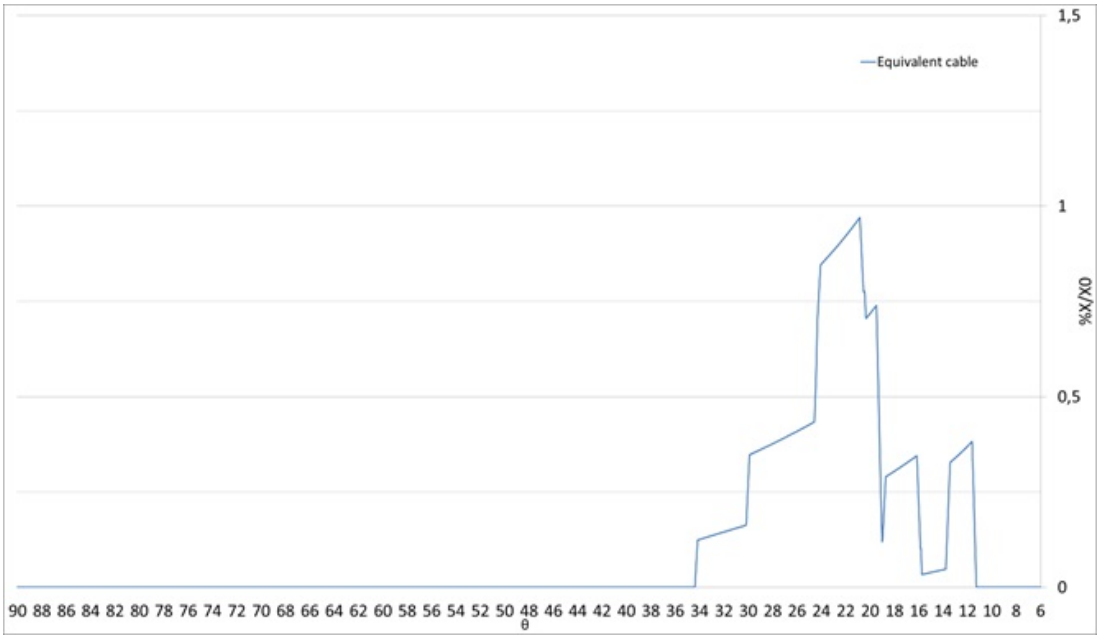


Figure 60: Contribution to the material budget of the cables in the vertex detector considering, for simplification purposes, an homogenized cable layout in $\Phi$.

In order to evaluate the relative contribution of each element to the total material budget, the curves in Figure 62 were integrated and the results shown in Figure 63 as a percentage of the total material budget. The CFRP support structures and silicon used in the sensors and ASICS are the components which contribute the most to the material budget (34% and 31%, respectively). Other important elements are the beryllium beam pipe and the components required for the power pulsing (LDOs, capacitors and flex cables), contributing to 12% and 13% of the total material budget, respectively. Finally, the adhesives (epoxy) and the cables outside the staves and petals contribute, in total, with 8% to the material budget.

The total calculated values of the material budget can be compared with the values used for the physics simulations in the CDR shown in Figure 54b. Figure 64 shows the results of this comparison. Furthermore, in order to compare the material budget in the engineering model with the CDR realistic targets presented in Table 9, a third curve was added to the graph in Figure 64. This curve corresponds to the physics simulations data scaled by 1.78 (the ratio between the material budget considering the CDR realistic target and the one used in the physics simulations for $\theta = 90^\circ$).

It can then be observed that the calculated values for the engineering model are near to the CDR realistic targets. However, it is important to note some observations:

- The transition between the barrel staves and the forward region starts about $5^\circ$ earlier in the engineering model ($\theta = 37.5^\circ$ vs. $\theta = 32.5^\circ$). This is due to the fact that in the physics simulations there is no support structure for the barrel staves.
- The material budget in the engineering model decreases between $\theta = 12.5^\circ$ and $\theta = 7^\circ$ while in the physics simulations there is an increase between these angles. This is due to the path chosen for the

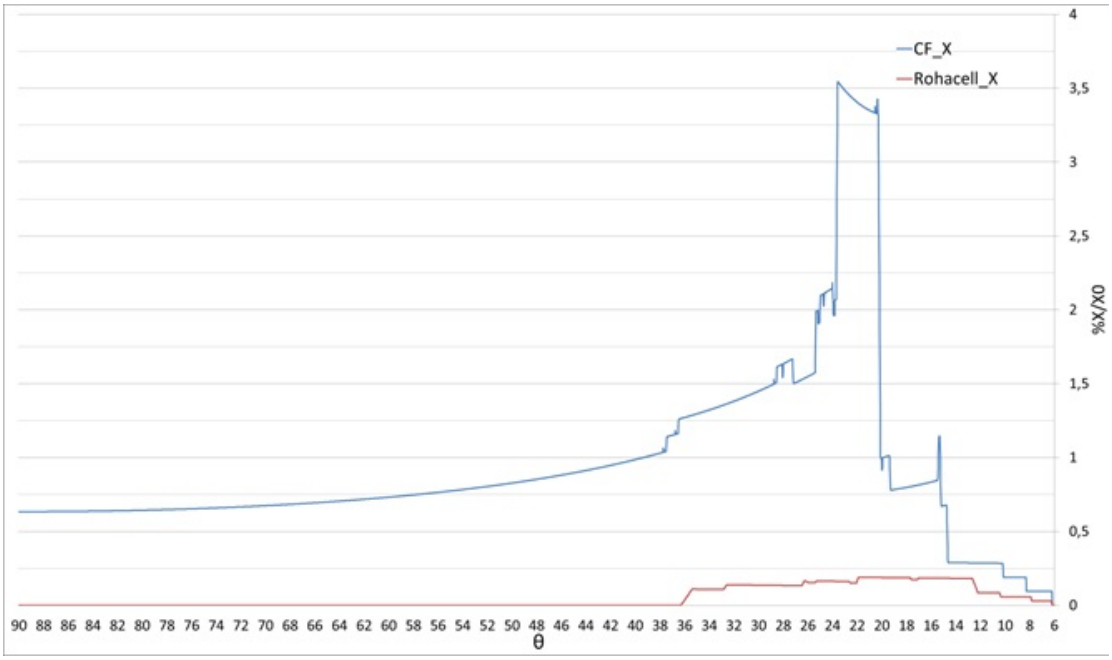


Figure 61: Contribution to the material budget of the different materials (CFRP and rohacell) that compose the support structures of the vertex detector, including the Inner Support Structure. Due to the density difference between CFRP and rohacell, the contribution of rohacell is small, despite the thicker elements, when compared to that of CFRP.

cable routing in this region. In the physics simulations the cables surround the beam pipe and, thus, are accumulated in the lower angles while in the engineering model they are routed along the Inner Support Structure. As a consequence, for lower angles, the material budget in the engineering model decreases.

If the material budget distribution along $\theta$ is integrated for both the engineering model and the CDR realistic targets, one can conclude that the material budget in the engineering model is 10% higher than the CDR targets (assuming that its distribution along $\theta$ corresponds to the physics simulation values scaled by a factor of 1.78).

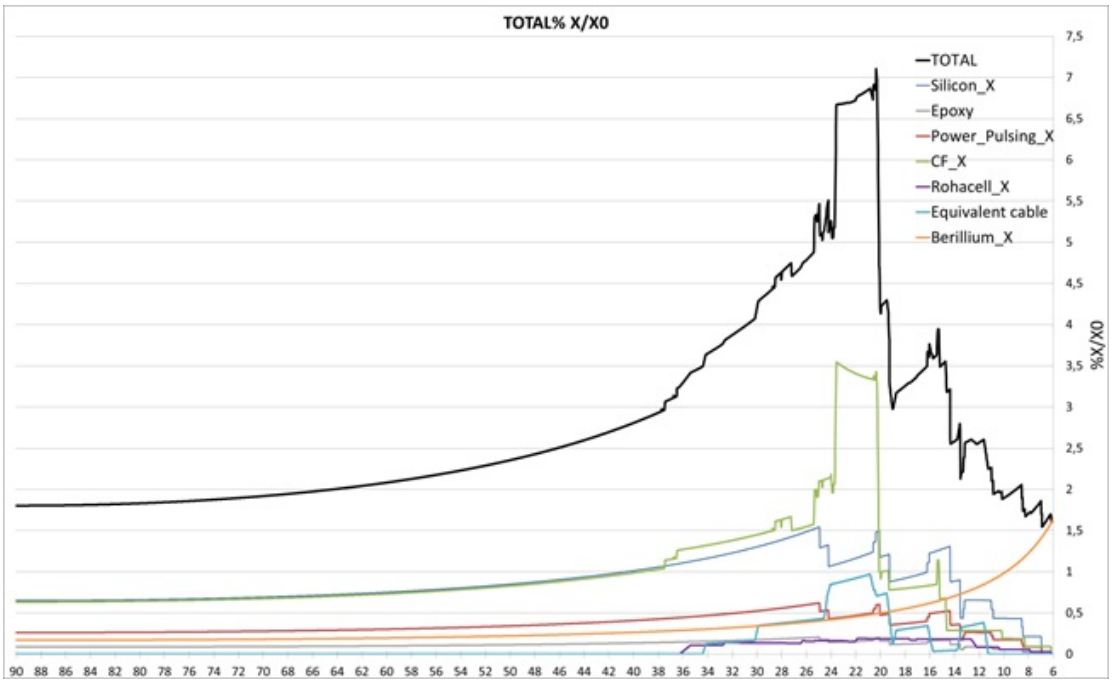


Figure 62: Total material budget in the vertex detector. Shown is also the individual contribution of each element. The CFRP support structures and the silicon are the components that contribute the most to the material budget.

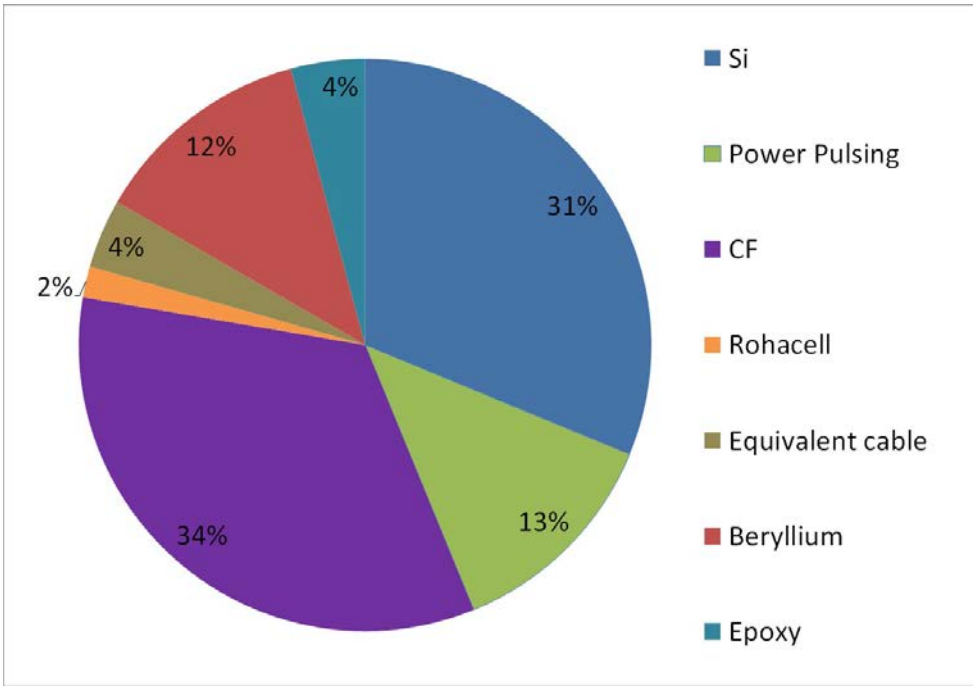


Figure 63: Contribution of the individual components to the total amount of material averaged over all polar angles from 6° to 90°.

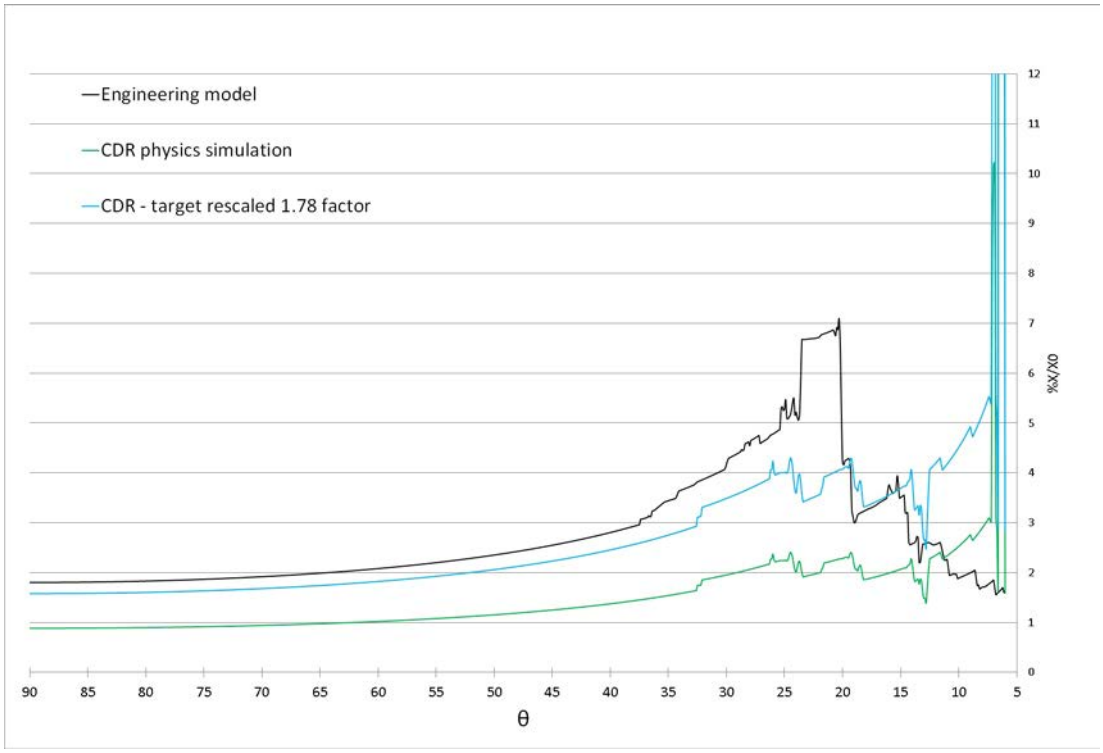


Figure 64: Comparison of the material budget values between the CDR physics simulations (in green), the CDR realistic target values (in blue) and the engineering model (in black).

### Material budget vs. $\Phi$

The CATIA plug-in was also used to obtain the material budget versus the angle $\Phi$, for $\theta = 90°$. The results are shown in Figure 65 where it can be seen that the values oscillate between 1.70% X/$X_0$ and 2.45% X/$X_0$.

The distribution of the material budget along $\Phi$ is irregular for two main reasons: the non cylindrical shape of the barrel results in different effective thicknesses depending on the angle of the tracks, and the overlapping of the sensors' edges increases the material budget in some specific angles. The comparison between the layout of the staves in the barrel and the peaks in the material budget at $\theta = 90°$ is shown in Figure 66. There are 16 major peaks corresponding to the VXBD 1-2 and 5-6 layers and 12 minor peaks corresponding to the VXBD 3-4 layers.

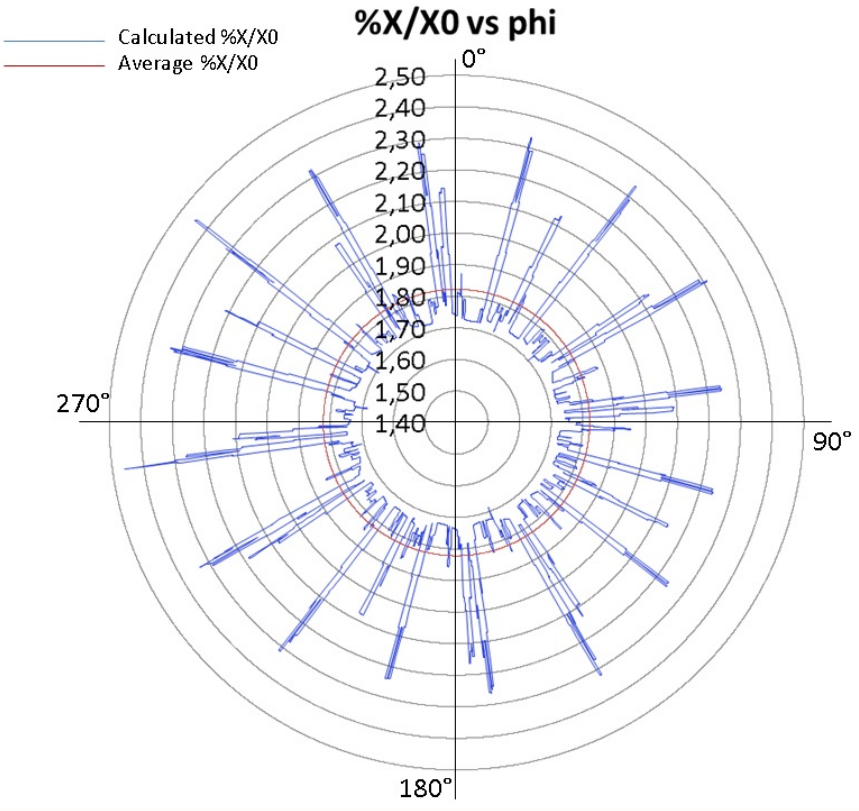


Figure 65: Material budget in the engineering model along the angle $\Phi$ for $\theta = 90°$ (in blue). The peak values occur were there is an overlap of the adjacent staves in a layer. The average material budget at $\theta = 90°$ is also plotted (in red) and has a value of 1.82% X/$X_0$.

Similarly to what was done for the angle $\theta$, it is also possible to quantify the contribution of each element to the material budget along the angle $\Phi$ (the average material budget at $\theta = 90°$ is $1.82\%X/X_0$). The relative contribution of each element is presented in Figure 67. As it can be seen, the 50 $\mu$m thick silicon sensor with the 50 $\mu$m thick ASIC in each VXBD layer has the biggest contribution to the total material budget (38%) closely followed by the CFRP support structure (33%). The absolute contribution of each CFRP structure in the barrel region is detailed in Table 15.

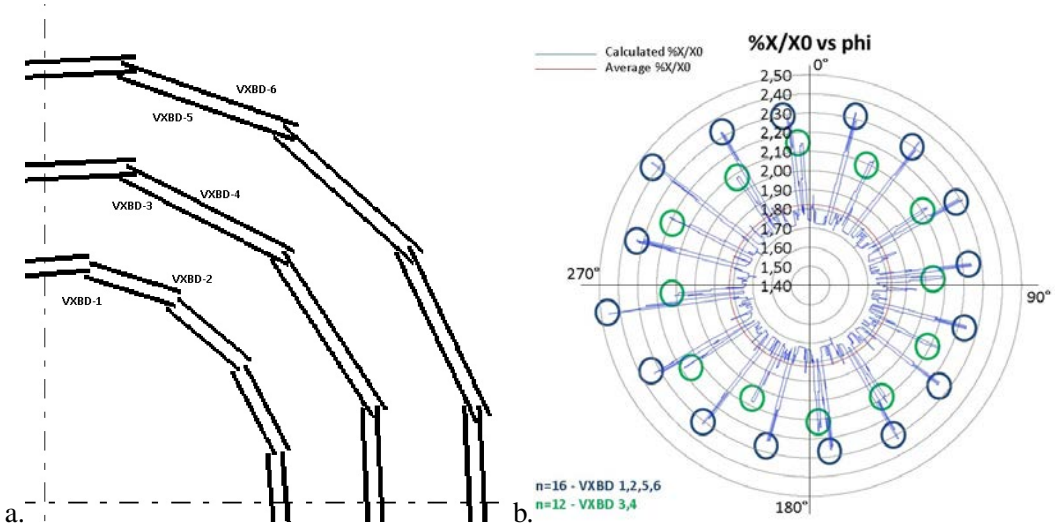


Figure 66: Comparison between a) the layout of the staves in the barrel and b) the peaks in the material budget at $\theta = 90^\circ$. The green circles correspond to the 12 peaks produced by the overlapping of the 12 staves that make the VXBD 3-4 layers while the blue circles correspond to the 16 peaks produced by the overlapping of the 16 staves that make the VXBD 1-2 and 5-6 layers.

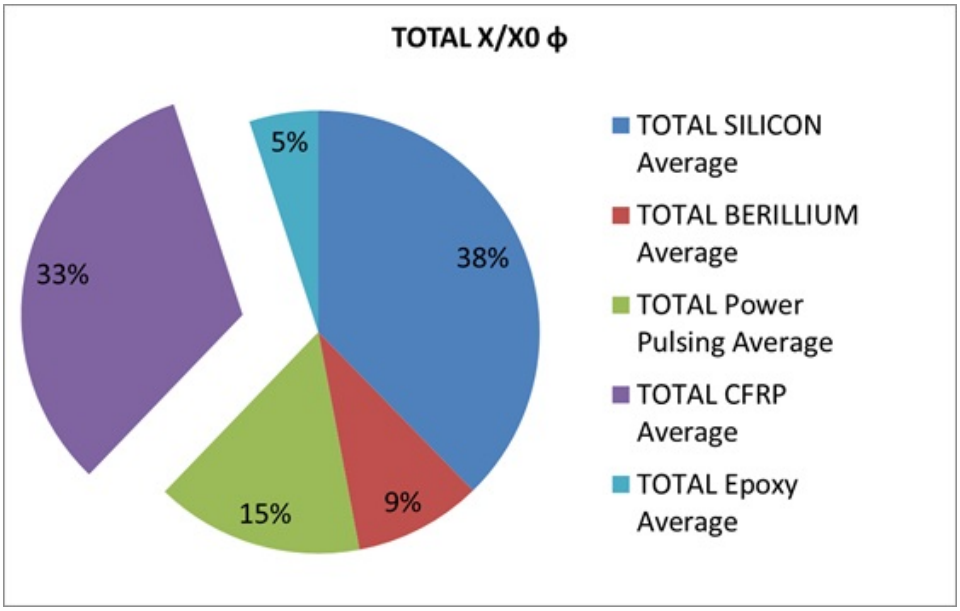


Figure 67: Relative contribution of each element to the total material budget in the engineering model at $\theta = 90^\circ$ (averaged over $\Phi$).

Table 15: Material budget of each CFRP structure in the vertex detector barrel region, at $\theta = 90^{\circ}$.

| Component | Thickness [mm] | Material Budget contribution [%X/$X_0$] |
|---|---|---|
| Inner Support Structure | 0.8 | 0.312 |
| Air-Flow Guiding Cylinder | 0.2 | 0.078 |
| Stave supports (3) | 0.1 (3) | 0.07 (3) |
| TOTAL | | 0.61 |

# 9 Appendix E: Acronyms

| | |
|---|---|
| **CAD** | Computer Aided Design |
| **CDR** | Conceptual Design Report |
| **CFRP** | Carbon Fiber Reinforced Polymer |
| **CLIC** | Compact Linear Collider |
| **FEA** | Finite Element Analysis |
| **FTD** | Forward Tracking Disk |
| **ILD** | International Linear Detector |
| **IP** | Interaction Point |
| **SIT** | Silicon Internal Tracker |
| **VXBD** | Vertex Barrel Detector/s |
| **VXD** | Vertex Detector/s |
| **VXEC** | Vertex Endcap/s |

## References


[1] L. Linssen, A. Miyamoto, M. Stanitzki, and H. Weerts,
*Physics and Detectors at CLIC:CLIC Conceptual Design Report.* (CERN-2012-003),
CERN, Geneva, 2012.

[2] F. Duarte Ramos, H. Gerwig and M.A. Villarejo Bermudez,
*CLIC inner detectors cooling simulations*, LCD-Note-2013-007 (2013).

[3] A. Munnich, A. Sailer,
*The CLIC ILD CDR Geometry for the CDR Monte Carlo Mass Production*,
LCD-Note-2011-002 (2012).

[4] D. Dannheim, A. Sailer, *Beam-Induced Backgrounds in the CLIC Detectors*,
LCD-Note-2011-021 (2012).

[5] TORAY CARBON FIBERS AMERICA, INC., *M55J Data Sheet*,
http://www.toraycfa.com/pdfs/M55JDataSheet.pdf.

[6] MATWEB, *Rohacell*, http://www.matweb.com.

[7] J. M. Rotter, H. Schmidt,
*Buckling of Steel shells European Design Recommendations-5th edition*, Eurocode 3, Part 1-6,
ECCS Press P-125,Brussels, 2008, ISBN: 92-9147-000-92.

[8] *Buckling Strength of Shells*, DNV-RP-C202, Det Norske Veritas, 2010.

[9] L. R. Center, *Buckling of Thin-walled Truncated Cones*, NASA space vehicle design criteria,
Clearinghouse for Federal Scientific and Technical Information, 1968,
URL: http://books.google.ch/books?id=z5nMGwAACAAJ.

[10] R. Roark, W. Young, R. Budynas, *Roark's Formulas for Stress and Strain*,
McGraw Hill professional, McGraw-Hill, 2002, ISBN: 9780071501811,
URL: http://books.google.ch/books?id=pummClLoFXEC.

[11] D. Brush, B. Almroth, *Buckling of bars, plates and shells*, International student edition,
McGraw-Hill, 1975, ISBN: 9780070327580,
URL: http://books.google.ch/books?id=OpgeMwEACAAJ.

[12] M. Anduze, H. Videau, M. Jore, *Note on the beam tube for ILD* (2009), URL: http://ilcild.org/documents/mdi/Beam_tube_note.pdf/at_download/file.

[13] M. A. V. Bermudez, F. D. Ramos,
*Cable bending simulations related to a CLIC detector cabling scheme*,
CLICdp-Internal-2014-001 (2014).

[14] G. Blanchot, D. Dannheim and C. Fuentes, *Power-pulsing schemes for vertex detectors at CLIC*,
Journal of Instrumentation **9** 01 (2014).

[15] F. Duarte Ramos, H. Gerwig and M.A. Villarejo Bermudez,
*CLIC ILD inner detectors cooling simulations*, LCD-Note-2013-007 (2013).

[16] D. Dannheim, M. Vos,
*Simulation studies for the layout of the vertex and tracking regions of the CLIC detectors*,
LCD-Note-2011-031 (2012).

[17] D. Laporte and Ph. Schwemling, *Material evaluation*, Oxford, 2013,
eprint: hep-ph/0306267.